The 3D biogeochemical marine mercury cycling model MERCY v2.0 – linking atmospheric Hg to methyl mercury in fish.

Johannes Bieser[1,*], David Amptmeijer[1], Ute Daewel[1] , Joachim Kuss[2], Anne L. Soerenson[3], Corinna Schrum[1,4],

[1] Helmholtz-Zentrum Hereon, Institute of Coastal Research, Max-Planck-Str. 1, 21502 Geesthacht, Germany
[2] Leibniz Institute for Baltic Sea research, Department for Marine Biogeochemistry, Seestraße 15, 18119 Rostock, Germany
[3] Swedish Museum of Natural History, Department of Environmental Research and Monitoring, Stockholm, Sweden
[4] Universität Hamburg, Institute for Marine Sciences, Mittelweg 177, 20146 Hamburg, Germany
[*] Correspondence to: Johannes Bieser (johannes.bieser@hereon.de)

Abstract

Mercury (Hg) is a pollutant of global concern. Due to anthropogenic emissions, the atmospheric and surface ocean Hg burden has increased substantially since preindustrial times. Hg emitted into the atmosphere gets transported on a global scale and ultimately reaches the oceans. There it is transformed into highly toxic methylmercury (MeHg) that effectively accumulates in the food web. The international community has recognized this serious threat to human health and in 2017 regulated Hg use and emissions under the UN Minamata Convention. Currently, the first effectiveness evaluation of the Minamata Convention is being prepared and, in addition to observations, models play a major role in understanding environmental Hg pathways and in predicting the impact of policy decisions and external drivers (e.g. climate, emission, and land-use change) on Hg pollution. Yet, the available model capabilities are mainly limited to atmospheric models covering the Hg cycle from emission to deposition. With the presented model MERCY v2.0 we want to contribute to the currently ongoing effort to improve our understanding of Hg and MeHg transport, transformation, and bioaccumulation in the marine environment with the ultimate goal of linking anthropogenic Hg releases to MeHg in sea food.

Here, we present the equations and parameters implemented in the MERCY model and evaluate the model performance for two European shelf seas, the North-and Baltic Sea. With the model evaluation we want to establish a set of general quality criteria that can be used for evaluation of marine Hg models. The evaluation is based on statistical criteria developed for the performance evaluation of atmospheric chemistry transport models. We show that the MERCY model can reproduce observed average concentrations of individual Hg species in water (normalized mean bias: Hg_T 17%, Hg^0 2%, MeHg -28%) in the two regions mentioned above. Moreover, it is able to reproduce the observed seasonality and spatial patterns. We find that the model error for $Hg_{T(aq)}$ is mainly driven by the limitations of the physical model setup in the coastal zone and the availability of data on Hg loads in major rivers. In addition, the model error in calculating vertical mixing and stratification contributes to the total Hg_T model error. For the vertical transport we find that the widely used particle partitioning coefficient for organic matter of $\log(k_d)=5.6$ is too low for the coastal systems. For Hg^0 the model performance is at a level where further model improvements will be difficult to achieve. For MeHg, our understanding of the processes controlling methylation and demethylation is still quite limited. While the model can reproduce average MeHg concentrations, this lack in understanding hampers our ability to reproduce the observed value range. Finally, we evaluate Hg and MeHg concentrations in biota and show, that modelled values are within the range of observed levels of accumulation in phytoplankton, zooplankton, and fish. The model performance demonstrates the feasibility of developing marine Hg models with similar predictive capability as established atmospheric chemistry transport models. Our findings also highlight important knowledge gaps in the dynamics controlling methylation and bioaccumulation that, if closed, could lead to important improvements of the model performance.

1 Background

Mercury (Hg) is a global pollutant and a dangerous neurotoxin (AMAP/UNEP, 2019). Since pre-industrial times, the global Hg cycle has been significantly altered by anthropogenic emissions (Streets et al., 2019) resulting in a three-fold pre-anthropogenic to present-day increase in the atmospheric and substantial increase in oceanic Hg burden (Lehnherr et al. 2015, Amos et al., 2013). The major anthropogenic sources of Hg are emissions from coal-fired power plants, small scale artisanal gold mining, and metal and cement production (Pirrone et al., 2010; AMAP/UNEP 2013, 2019). In addition, natural emissions and legacy reemissions from previously deposited Hg (most of it of anthropogenic origin) also contribute significantly to the atmospheric Hg burden (Pirrone et al., 2010; Driscoll, 2013; Obrist, 2018). The atmospheric lifetime of Hg is estimated in the range of 0.6 and 1.0 years (Slemr et al., 2018) resulting in a global atmospheric distribution of Hg. Atmospheric Hg will eventually deposit (Cohen et al., 2016; Jiskra et al., 2018). A large fraction is deposited directly to the ocean but Hg deposited to land can also be transported to the ocean via rivers and groundwater. In the aqueous phase, inorganic Hg can be methylated forming the highly bioaccumulative monomethylmercury (MMHg) and/or dimethylmercury (DMHg). These MeHg compounds are readily accumulated in the food web and pose a risk to food safety and human health (Clarkson, 1990; Mason et al., 1996; Chen et al., 2012; Parks et al., 2013; Puty et al., 2019). Because of this, the international community, under the umbrella of the United Nations Environmental Program (UNEP), signed the Minamata Convention on Mercury which came into force in 2017. Under this convention, all participating 184 nations have agreed to assess Hg pollution under their jurisdiction, to minimize usage and release of Hg compounds into the environment, and to regularly assess the impact of the reduction measures taken on environmental Hg burden and distribution. In order to assess the impact of reduction measures, there is an urgent need to understand the Hg pathways from anthropogenic releases to top predators and humans, with a specific attention to the marine ecosystem.

In this manuscript, we (1) introduce a newly developed numerical multi-compartment model for Hg cycling in the marine environment including accumulation in the marine food-web (MERCY v2.0) and (2) evaluate the model performance to reproduce observed concentrations, seasonality, and variability of Hg species. For the latter, we apply performance criteria used for evaluation of atmospheric chemistry transport models also for evaluation of marine Hg models. We use these criteria to (2.1) quantify the models predictive capabilities based on our current understanding of Hg cycling, to (2.2) identify the major sources of model error, and to (2.3) quantify the constraints on model improvement based on current process understanding and measurement availability and uncertainty. With this study, we present an evaluation of our marine Hg model and a general framework that provide the basis for future intercomparison studies of marine Hg models.

1.1 Research question

The key question concerning Hg pollution is how changing Hg emissions and other external stressors such as climate and land-use change impact MeHg accumulation in sea food which is an important global protein source for human consumption (Pauly et al., 2002; Obrist et al., 2018). To anticipate the natural Hg cycle and to identify the impact of human actions on the system it is necessary to develop multi-compartment chemistry transport models (CTMs) including all relevant compartments: atmosphere, soil/vegetation, rivers and oceans, sediments, and the marine ecosystem. The need to incorporate all compartments into a single multi-compartment model arises from the fact that Hg is non-degradable and constantly cycling between environmental compartments, unlike most pollutants which tend to accumulate in a single compartment and/or degrade over time. For example, atmospheric deposition of oxidized Hg is a major flux of Hg into the ocean but reduction reactions in the ocean and the high vapour pressure of elemental Hg^0

also result in a constant release of Hg from ocean to atmosphere (Fitzgerald et al., 1984; Kim and Fitzgerald, 1986; Andersson et al., 2008). The only real sink for Hg in the environment is burial in the lithosphere mainly as stable cinnabar (HgS) in anoxic marine sediments. Thus, coupled earth system models are needed to gain a deeper understanding of the processes and dynamics governing transport of Hg, Hg methylation and the variability of Hg accumulation in the marine food web. While there is a large number of emission inventories and atmospheric CTMs, there are still only a limited number of CTMs with a focus on the marine Hg cycling and food web transfers.

1.2 Development and state-of-the-art in Hg modelling

Atmospheric Hg modelling is well established and a large variety of global (ECHMERIT: Jung et al., 2009; De Simone et al, 2014; GLEMOS: Travnikov and Ilyin, 2009; Travnikov et al., 2009; GEM-MACH: Dunfoord et al., 2012; Kos et al., 2013; Dastoor et al., 2015; GEOS-Chem: Holmes et al., 2010; Amos et al., 2012; Song et al., 2015) and regional (CMAQ: Bullock et al., 2008; Bash et al., 2010; Zhu et al., 2015, DEHM: Chritensen et al., 2004; WRF-Chem: Gencarelli et al., 2017) atmospheric CTMs for Hg cycling have been published. Due to this abundance, many model inter-comparison and source apportionment studies have improved our understanding of atmospheric Hg transport, source receptor relationships and allowed us to predict future atmospheric Hg levels and deposition fluxes (Bergan et al., 1999; Xu et al., 2000; Petersen et al., 2001; Lee et al., 2001; Seigneur et al., 2001; Bullock et al., 2002; Dastoor et al., 2002; Hedgeock et al., 2004; Selin et al., 2007; Travnikov et al., 2009; Bieser et al., 2014; Gencarelli et al., 2014; Dastoor et al., 2015; Song et al., 2015; Cohen et al., 2016; Travnikov et al., 2017; Bieser et al., 2017; Horowitz et al., 2017). These models and studies are a keystone in informing policy makers to support the implementation and effectiveness evaluation of the Minamata Convention (http://www.mercuryconvention.org).

Compared to Hg modelling in the atmosphere, marine Hg modelling is still in its infancy and only a limited number of models exist so far. The development of marine Hg models can be divided in to four phases. At first, the ocean was implemented as a boundary for atmospheric CTMs and nowadays most atmospheric CTMs implement some kind of surface ocean parametrization to explicitly include Hg air-sea exchange. One of the earliest marine Hg model developments was the addition of inorganic Hg red-ox chemistry and transport in a 2D slab ocean model coupled to the GEOS-Chem model (Selin et al., 2008; Strode et al., 2007; Soerensen et al., 2010). The aim of these early models was to improve air-sea exchange by including horizontal transport, red-ox chemistry, and river loads. Next, came the development of the first marine 3D models. These models, still limited to the inorganic Hg cycle, were used to investigate marine Hg dynamics (Zhang et al., 2014a; Zhang et al. 2014b; Bieser and Schrum 2016). In the next stage, several specialized marine Hg models were developed which were not based on 3D hydrodynamic models. Soerensen et al. (2016) published a coupled physical-biogeochemical multi-box model including organic Hg chemistry to investigate the Hg budgets in the Baltic Sea. Focusing on bioaccumulation Schartup et al. (2017) implemented Hg accumulation in a complex food web model and Sunderland et al. (2018) modelled the consumer exposure to MeHg in sea food. Finally, Pakhomova et al. (2018) developed a model with comprehensive Hg chemistry based on a hydrodynamic 1D model. Only in recent years has the development of comprehensive marine Hg models gained traction. So far, four marine Hg models based on numerical hydrodynamic 3D models have been published (Semeniuk et al., 2017; Zhang et al., 2019; Kawai et al., 2020; Rosati et al., 2022). All of these models include a complete marine Hg chemistry including MeHg. Yet, only Zhang et al. (2020) and Rosati et al. (2022) also implemented Hg cycling into a biogeochemical model considering uptake to and release from marine biota, making it the first hydrodynamic 3D Hg model to include the marine ecosystem.

1.3 Our contribution to the presented problem

Here we present our newly developed biogeochemical multi-compartment model for Hg cycling MERCY v2.0 and evaluate its predictive capabilities and limitations using evaluation criteria applied for performance evaluation of atmospheric CTMs (Derwent et al., 2010; Thunis et al., 2012; 2013; Carnevale et al., 2014). We focus on the implementation of the marine Hg cycle including a comprehensive marine Hg chemistry and partitioning scheme as well as bio-concentration and bio-magnification. We improve on the state-of-the-art by introducing an experimental upper trophic layer that simulate Hg and MeHg accumulation in fish. To our knowledge, MERCY v2.0 includes all currently known processes controling marine Hg cycling. The model is based purely on processes, reactions, and rates published in peer reviewed literature and no additional model tuning was performed.

We investigate the model predictive capabilities, something we consider important before using the model to study budgets or global dynamics. This allows us to quantify our model uncertainty, which for other models has only been loosely constrained to be *'orders of magnitude'* (Kawai et al., 2020), and discuss the processes and parameters driving it. Set up on a high-resolution regional domain covering a wide range of marine regimes in a region with high primary productivity and a relative abundance of observations we evaluate the ability to reproduce observed concentrations, seasonality, and variability of individual marine Hg species. Using common practice from atmospheric Hg modelling, we establish a quantitative benchmark for the capability of the model to reproduce actual observations of marine Hg concentration and speciation. Based on this we discuss the major knowledge gaps and research questions that need to be tackled in order to improve our understanding of marine Hg cycling. Our ultimate goal is to improve capabilities to link changes in external stressors like anthropogenic emissions and climate change to MeHg accumulation in the marine food web by providing an independent model for marine Hg cycling and by fostering collaboration in the form of model inter-comparison studies comparable to the efforts in atmospheric Hg modelling (Ryaboshapko et al., 2002; Bullock et al., 2008; Travnikov et al., 2017; Bieser et al., 2018). Finally, we want to identify and communicate the major needs for monitoring of Hg species in the marine environment.

2 Model description

2.1 Model Framework

The marine Hg chemistry scheme we develop for MERCY v2.0 is embedded in to GCOAST (Geesthacht Coupled cOAstal model SysTem), a modelling framework coupling physical, chemical, and biological numerical models. It is an update and overhaul of MERCY v1.0 (Bieser and Schrum, 2016) which featured only inorganic Hg chemistry and no ecosystem interactions. As input, MERCY uses hourly model output from four types of 3D hydrodynamic models (atmospheric physics, atmospheric chemistry, marine physics and marine ecosystem) to drive the marine Hg speciation, transport, and bioaccumulation model. While this approach requires a large amount of storage capacity, it reduces the computational requirements and allows the model to be easily run with input from alternative biogeophysical models. The external variables used by MERCY are listed in Table 1. In brief, models used in this work are:

(1) The regional weather and climate model **COSMO-CLM** (Rockel und Geyer, 2008) provides meteorological variables used to calculate air-sea exchange (temperature and wind speed) and photolytic reactions (surface short wave radiation).

(2) The atmospheric chemistry transport model **CMAQ-Hg** (Buyn and Schere, 2006; Zhu et al., 2015; Bieser et al., 2016) is forced by COSMO-CLM meteorology and used to calculate atmospheric transport, chemistry, particle partitioning, and deposition for atmospheric trace gases. MERCY uses atmospheric Hg concentrations and deposition fluxes from CMAQ-Hg.

(3) The physical hydrodynamic ice-ocean model **HAMSOM** (Backhaus et al., 1984, Schrum and Backhaus, 1999). HAMSOM is directly coupled to the ecosystem model ECOSMO enabling it to represent the impact of the ecosystem on the hydrodynamics (e.g. light attenuation by biota). In MERCY the physical variables are used to calculate marine mercury transport as well as temperature and salinity dependence of mercury cycling and speciation. The HAMSOM advection scheme is used to transport all Hg state variables.

(4) The marine end-to-end NPZD (Nutrient Phytoplankton Zooplankton Detritus) ecosystem model **ECOSMO** (Schrum et al., 2006, Daewel and Schrum, 2013, Daewel et al. 2019). ECOSMO is a 3D resolved food web model directly coupled with HAMSOM. It includes nutrients (nitrogen, phosphorus, and silica) and a food web based on a functional group approach with 3 phytoplankton species (diatoms, flagellates, and cyanobacteria), 2 zooplankton species (herbivore and omnivore), a macrobenthos and a pelagic fish group representing higher trophic levels. Additionally, oxygen, biogenic opal, detritus, and dissolved organic matter are considered, and the model includes a two-layer sediment compartment to simulate sedimentation and resuspension. In MERCY detritus and dissolved organic matter determine the partitioning of Hg and MeHg and factors such as light attenuation and oxygen concentration influence Hg speciation. Moreover, concentrations of the various species of the model food web are used to calculate bioconcentration and biomagnification of Hg and MeHg.

All employed models are freely available (see 'Code Availability' section at the end of the manuscript).

#	Name	Description	Unit	Source model
1	T_a	Air temperature	°C	COSMO-CLM
2	U_{10}	Wind speed at 10m	m s^{-1}	COSMO-CLM
3	RSRF	Shortwave radiation at surface	W m^{-2}	COSMO-CLM
4	GEM	(Gaseous Elemental Mercury) Atmospheric Hg^0 concentration	ng m^{-3}	CMAQ-Hg
5	GOM	(Gaseous Oxidized Mercury) $Hg^{2+}_{(g)}$ (GOM) deposition	kg ha^{-1}	CMAQ-Hg
6	PBM	(Particulate Bound Mercury) $Hg_P{}^{2+}_{(s)}$ (PBM) deposition	kg ha^{-1}	CMAQ-Hg
7	T_w	Water temperature	°C	HAMSOM
8	rho	Water pressure	Pa	HAMSOM
9	U_w	Water U-velocity	m s^{-1}	HAMSOM
10	V_w	Water V-velocity	m s^{-1}	HAMSOM
11	S	Salinity	PSU	HAMSOM
12	dh_0	Surface layer elevation	m	HAMSOM
13	FLA	Flagellate biomass	mgC m^{-3}	ECOSMO
14	DIA	Diatom biomass	mgC m^{-3}	ECOSMO
15	CYA	Cyanobacteria biomass	mgC m^{-3}	ECOSMO
16	ZOS	Herbivorous zooplankton biomass	mgC m^{-3}	ECOSMO
17	ZOL	Omnivorous zooplankton biomass	mgC m^{-3}	ECOSMO
18	FSH	Fish biomass	mgC m^{-3}	ECOSMO
19	MAC	Macro benthos biomass	mgC m^{-2}	ECOSMO
20	DOC	Dissolved Organic Carbon concentration	mgC m^{-3}	ECOSMO
21	POC	Particulate Organic Carbon concentration	mgC m^{-3}	ECOSMO
22	STOT	Sediment load	mgC m^{-2}	ECOSMO
23	RTOT	Resuspended sediment	mgC m^{-2}	ECOSMO
24	O_2	Oxygen concentration	mgC m^{-3}	ECOSMO
25	SO_4^{2-}	Sulphate concentration	mgC m^{-3}	ECOSMO
26-28	P_x	3 × Production rates for phytoplankton species (x)	mgC cm^{-3} s^{-1} *	ECOSMO
29-46	$F_{x,y}$	17 × Feeding rates for biological species (x) on species (y)	mgC cm^{-3} s^{-1} *	ECOSMO
47-54	M_x	7 × Mortality rates for biological species (x)	mgC cm^{-3} s^{-1} *	ECOSMO

*Table 1: MERCY input variables and source models. (*rates for macro benthos are in mgC m^{-2} s^{-1}).*

2.2 General Equations

MERCY v2.0 implements all processes we identified as relevant for marine (pelagic and benthic) Hg cycling into a 3D ocean-ecosystem model. MERCY is based on basic principles describing Hg transport, transformation, and bioaccumulation. It is set up on the same grid and domain as the coupled ocean ecosystem model ECOSMO-HAMSOM. Based on archived hourly ECOSMO-HAMSOM output, it is effectively offline coupled to the marine hydrodynamic and ecosystem models. The ECOSMO-HAMSOM model has been shown to accurately reproduce ecosystem dynamics in the coupled North Sea-Baltic Sea system. The model equations and a model validation on the basis of nutrients are presented in detail by Daewel and Schrum (2013), who showed that the model can reasonably simulate ecosystem productivity in the North Sea and the Baltic Sea on seasonal up to decadal timescales. Using the same numerical approximations as described in Daewel (2019) the rate of change in concentration of Hg state variables over time $\frac{\delta C}{\delta t}$ is estimated by the prognostic equation (Eq. 1). This rate of change is subsequently integrated over the internal timestep and applied to the corresponding state variables.

$$\frac{\delta C}{\delta t} = V \nabla C + w_d \frac{\delta C}{\delta z} + \frac{dz}{\delta z}\left(A_v \frac{\delta C}{\delta z}\right) + R_{(C,B)} \qquad \text{Eq. 1}$$

The physical transport terms for advection $V \nabla C$ with 3D velocity field $V=(u,v,w)$, vertical transport $w_d \frac{\delta C}{\delta z}$ with sinking velocity w_d, and turbulent mixing $\frac{dz}{\delta z}\left(A_v \frac{\delta C}{\delta z}\right)$ with diffusion coefficient A_v and velocity V are calculated by the hydrodynamic host model. At the upper and lower boundary of the water column, boundary conditions are presented to account for air-sea exchange (Section 2.3.6) and sedimentation and resuspension (Section 2.3.5). Each Hg state variable C is subject to additional transformations $R_{(C,B)}$ which include chemical transformations $Rc_{(C)}$ (Section 2.3.1), partitioning $Rp_{(C)}$ (Section 2.3.2), and biological uptake $Rb_{(C,B)}$ by ecosystem group B (Section 2.3.4) (Eq. 2). Marine biota is implemented in the ecosystem model following a functional group approach further described in Section 2.3.4. All transformations $R_{(C,B)}$ are mass conserving transfer reactions which means that besides emission inputs and inflow/outflow at the domain boundaries no Hg is added or removed from the system. The exact formulation of $R_{(C,B)}$ differs for each Hg species in the model. In this section, we give a general overview of all possible transformations while the exact formulae and parametrizations are given in Section 2.3. A complete list of all Hg state variables is given in Table 2. All chemical reactions $Rc_{(C)}$ and their respective reaction rates can be found in Table 3 and further physical and biological parameters are given in Table (4).

$$R_{(C,B)} = Rc_{(C)} + Rp_{(C)} + Rb_{(C,B)} \qquad \text{Eq. 2}$$

Chemical transformations $\mathrm{Rc}_{(C)}$ (Eq. 3) are the sum of all reactions where species C is a reaction product $\sum_{i=0}^{n} k_i C_i$ of another species C_i with reaction rate k_i minus the sum of all reactions where C is an educt $\sum_{j=0}^{n} k_j C$ with reaction rate k_j. Chemical reactions are implemented as pseudo 1st order reactions $\frac{\delta C}{\delta t} = kC$ either using a fixed reaction rate k_1 or a dynamic reaction rate $k_2 = k_1 C_2$ dependent on a second reactant C_2 or an associated environmental variable (e.g. temperature). For photolytic reactions the reaction rate is $k = k_p E_\lambda$ with the integrated photon flux $E_\lambda = \int_{\lambda_0}^{\lambda_n} E_\lambda$ for specific wavelengths λ and the photolysis rate k_p.

$$\mathrm{Rc}_{(C)} = \sum_{i=0}^{n} k_i C_i - \sum_{j=0}^{n} k_j C \qquad \text{Eq. 3}$$

n = number of Hg species

Partitioning $\mathrm{Rp}_{(C)}$ (Eq. 4) describes sorption and desorption of dissolved C_{aq} to particulate organic matter POM and dissolved organic matter DOM where C_{POM} is particulate $Hg^{2+}_{(s)}$ and C_{DOM} $Hg^{2+}_{(aq)}$ bound to DOM. The equilibrium between these species is described by sorption and desorption rates k_s and k_d.

$$Rp_{(c)}(C_{aq}) = k_d C_{POM} + k_d C_{DOM} - k_s C_{aq} POM - k_s C_{aq} DOM \qquad \text{Eq. 4.1}$$

$$Rp_{(c)}(C_{POM}) = k_s C_{aq} POM - k_d C_{POM} \qquad \text{Eq. 4.2}$$

$$Rp_{(c)}(C_{DOM}) = k_s C_{aq} DOM - k_d C_{DOM} \qquad \text{Eq. 4.3}$$

Biological uptake of Hg into biota $\mathrm{Rb}_{(C,B)}$ (Eq. 5) includes two distinct processes: (1) bio-concentration, which is defined as the passive uptake of dissolved $Hg^{2+}_{(aq)}$ through the cell membrane of a functional ecosystem group B and (2) bio-magnification, which is the sum of active uptake and release through feeding. For higher trophic levels, the Hg in biota from active and passive uptake is stored in separate state variables with different release rates due to the differing accumulation patterns for each uptake process.

$$\mathrm{Rb}_{(C,B)} = \sum_{i=0}^{n} (v_i A_B C_i) + \sum_{b=0}^{m} (r_{B,b} \epsilon_C C_b - r_{b,B} C_B) - (r_{r(B)} + r_{m(B)}) C_B \qquad \text{Eq. 5}$$

n = number of Hg species m = number of ecosystem groups

Bioconcentration $\sum_{i=0}^{n}(v_i A_b C_i) - r_r C_b$ is the sum of passive uptake with an uptake rate $r_u = v_i A_b$ depending on the permeation velocity v_i of dissolved Hg species C_i and the average ecosystem group surface area A_b minus an ecosystem group and Hg species-dependent release rate r_r multiplied with the Hg concentration inside biota C_b .

Biomagnification $\sum_{b=0}^{m} r_{B,b}\epsilon_C C_b - r_{b,B} C_B$ describes the active transfer of Hg driven by feeding rates $r_{B,b}$ of an ecosystem group B on other ecosystem groups b and the corresponding feeding pressure $r_{b,B}$. The efficiency of Hg transfer upon feeding is determined by a Hg species-dependent uptake efficiency ϵ_C .

Additional release from the biological matrix C_b is described by a mortality rate r_m . For the release of Hg from detritus into the dissolved Hg pool r_m is a temperature-dependent remineralization rate k_{rem} (see Eq. 9 in Section 2.3.1).

Finally, the respective change of dissolved Hg concentrations C_{aq} due to uptake into and release from marine biota is given by Eq. 6, where $\sum_{b=0}^{m} r_{B,b}(1-\epsilon_C) C_b$ is the Hg fraction directly excreted into the dissolved phase upon feeding of ecosystem group B on another ecosystem group b and $(r_{r(B)} + r_{r(B)}) C_B$ is the release due to a constant release rate $r_{r(B)}$ and the mortality rate $r_{m(B)}$ of Hg species C_b in ecosystem group B .

$$Rb_{(C,B)} = \sum_{b=0}^{m}\{r_{B,b}(1-\epsilon) C_b\} - \sum_{i=0}^{n}\{v_i A_B C_i\} + (r_{r(B)} + r_{m(B)}) C_B \qquad \text{Eq. 6}$$

n = number of Hg species, m = number of ecosystem groups

2.3 Implemented Processes

MERCY implements Hg using 35 variables (Table 2) representing different Hg species in the atmosphere, ocean, and sediment. For each model time step and each grid cell, the species are redistributed accounting for mass conservation based on physical, chemical, and biological processes. Figure 1 gives a graphical overview of transformations between Hg species in MERCY.

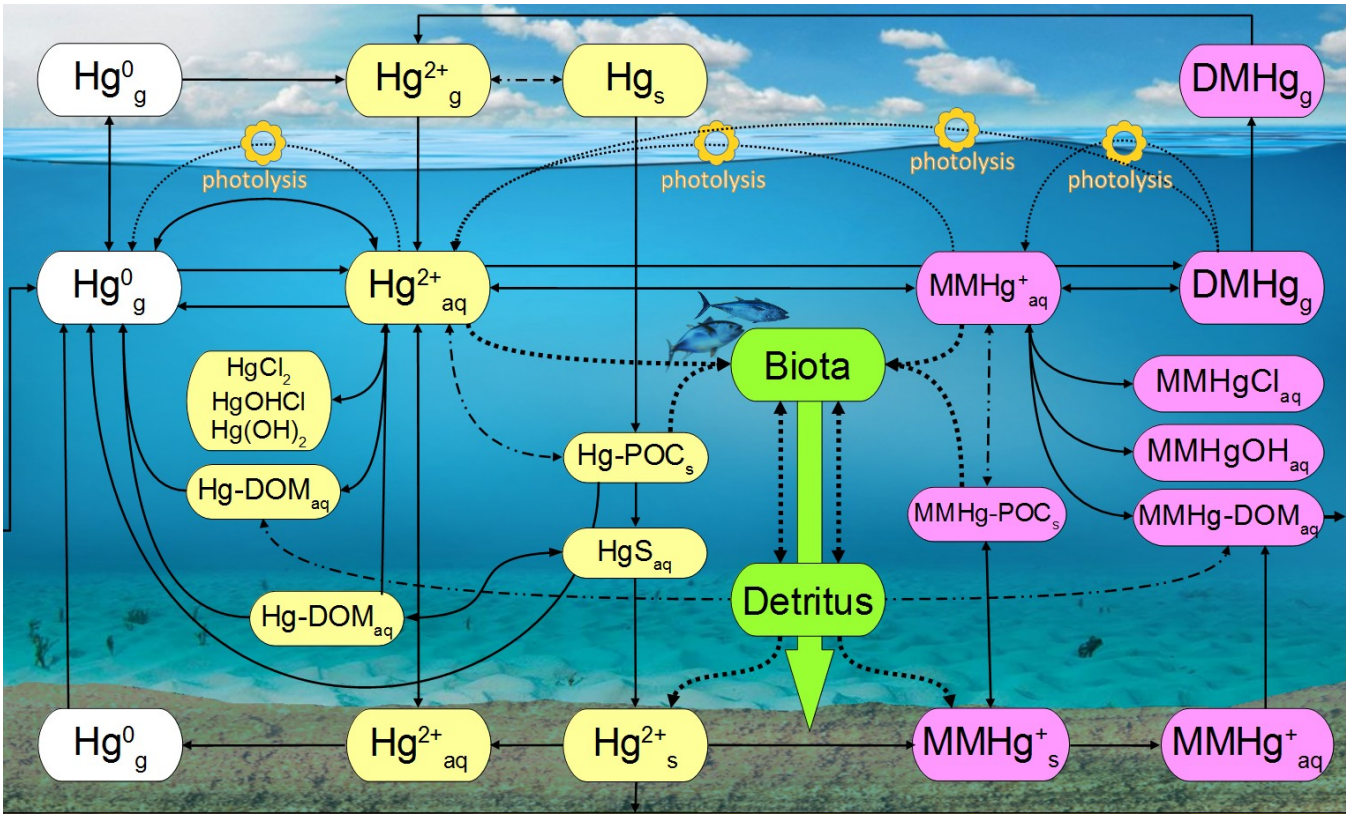

Figure 1: Schematic of the chemical mechanism in MERCY. Solid lines indicate chemical reactions, fine dotted lines photolytic reactions, dash-dotted lines instantaneous partitioning processes, bold dotted lines bioaccumulation and releases from biota into the dissolved phase. Colors codes are white for elemental mercury, yellow for inorganic oxidized mercury, pink for methylated mercury, and green for Hg in biota. The physical state of each species is indicated by: (g) for gaseous, (aq) for dissolved, and (s) for solid. The upper row indicates Hg species in the atmosphere, and the lower row those in the sediment. All species and their reactions are given in Table 2 & 3. Note reaction R20 reductive methylation (Table 3) MMHg-DOM → Hg^0 extends to the left edge of the figure.

Nr.	Species	Description	State	Compartments
1-2	$Hg^0_{(g)}$	gaseous elemental mercury	gaseous	atmosphere, water
3	$Hg^{2+}_{(g)}$	gaseous oxidized mercury	gaseous	atmosphere
4	$Hg_{(s)}$	mercury bound to particulate matter	solid	atmosphere
5-6	$Hg\text{-}POC_{(s)}$	mercury bound to particulate matter	solid	atmosphere, water, sediment
7-13	$Hg^{2+}_{(s)}$	dissolved oxidized mercury accumulated inside biota	solid	biota* (see Section 2.3.4)
14-17	$Hg^{2+}_{(s)}$	dissolved oxidized mercury attached onto biota	solid	biota* (see Section 2.3.4)
18	$Hg(OH)_{2(aq)}$	mercury hydroxide	dissolved	water
19	HgOHCl	Mercury hydroxy chloride	dissolved	water
20	$Hg(Cl)_{2(aq)}$	mercury chloride	dissolved	water
21	$Hg\text{-}DOM_{(aq)}$	mercury bound to dissolved organic matter	dissolved	water
22	$HgS_{(s)}$	cinnabar	solid	water
23	HgS-DOM	cinnabar bound to dissolved organic matter	dissolved	water
24	$MMHg^{+}\text{-}POC_{(s)}$	methyl mercury bound to particulate organic matter	solid	water
25-31	$MMHg^{+}_{(aq)}$	dissolved methyl mercury accumulated inside biota	solid	biota* (see Section 2.3.4)
32-35	$MMHg^{+}_{(aq)}$	dissolved methyl mercury attached onto biota	solid	biota* (see Section 2.3.4)
36	$MMHgOH_{(aq)}$	methyl mercury hydroxide	dissolved	water
37	$MMHgCl_{(aq)}$	methyl mercury chloride	dissolved	water
38	$MMHg\text{-}DOM_{(aq)}$	methyl mercury bound to dissolved organic matter	dissolved	water
39-40	$DMHg_{(g)}$	dimethyl mercury	gaseous	atmosphere, water

*Table 2: Hg species in MERCY. Species can represent state variables in multiple models. *Hg species in biota ($Hg^{2+}_{(s)}$ and $MMHg^{2+}_{(s)}$) represent one state variable for each functional group in the ecosystem model ECOSMO (see Section 2.3.4) giving a total of 40 species.*

2.3.1 Chemistry

In this section, we present all chemical state variables and the transformation processes in the model. A complete overview of all chemical transformations and the respective reaction rates k is given in Table 3. All chemical transformations are calculated using pseudo-first-order reactions following Equation 7. The chemical mechanism is implemented using a tendency approach, where the relative change for each reaction is calculated and all changes to state variables are applied simultaneously. Equation 3 gives the change to the concentration of a single Hg species due to all reactions depleting and producing it. We run the chemistry module with a time step of 60 s but find that it runs stable and efficient even with much larger time steps of 600 s.

$$C_t = C_0 e^{-t\,k} \qquad \text{Eq. 7}$$

C_t = Concentration at time = t [ng/L]

C_0 = Concentration at time = 0 [ng/L]

t = time [s]

k = pseudo-first order reaction constant [s^{-1}]

Nr.	Reaction	Description	Rate constant (k_1)	Source
R1	$Hg^{2+} \rightarrow Hg^0$	chemical (dark) reduction[1]	3.00E-07 [s^{-1}] @ 0°C 6.00E-07 [s^{-1}] @ 15°C 7.50E-07 [s^{-1}] @ 20°C	Kuss et al., 2015 (see Eq. 8)
R2	$Hg^{2+} + phot \rightarrow Hg^0$	photolytic reduction	1.00E-08 [m^2 W-1 s^{-1}]	Kuss et al., 2015
R3	$Hg^{2+} \rightarrow Hg^0$	biogenic reduction[2]	8.06 E-09 [m^3 $mg(C)^{-1}$ s^{-1}]	Kuss et al., 2015
R4	$Hg^0 \rightarrow Hg^{2+}$	chemical (dark) oxidation	2.60E-06 [s^{-1}]	Kuss et al., 2015
R5	$Hg^0 + phot \rightarrow Hg^{2+}$	photolytic oxidation[3]	0.24E-08 [m^2 W^{-1} s^{-1}]	Kuss et al., 2015
R6	$Hg^{2+} + H_2S \rightarrow HgS + 2H^+$	cinnabar formation[4]	4.90E-04 [m^3 $mg(S^{2-})^{-1}$ s^{-1}]	Slowey, 2010
R7	$HgS + DOM \rightarrow HgS\text{-}DOM$	cinnabar dissolution	5.78E-06 [s^{-1}]	Jiang, 2016
R8	$HgS\text{-}DOM_{(aq)} \rightarrow HgS_{(s)}$	re-crystallisation	9.50E-06 [s^{-1}]	Jiang, 2016
R9	$HgS + O_2 \rightarrow Hg^{2+} + 2SO_4^{2-}$	cinnabar oxidation[5]	1.00E-04 [m^3 $mg(O_2)^{-1}$ s^{-1}]	Petrochowa, 2019
R10	$Hg^{2+} \rightarrow MMHg^+$	anoxic methylation	4.40E-07 - 2.21E-07 [s^{-1}]	Monperuss et al., 2007 Duran et al., 2008 Lehnherr et al., 2011 Olsen et al., 2018 Soerensen et al., 2018
R11	$Hg^{2+} \rightarrow MMHg^+$	constant methylation	3.47E-08 [s^{-1}]	
R12	$Hg^{2+} \rightarrow MMHg^+$	biogenic methylation	4.05E-09 [l $mg(C)^{-1}$ s^{-1}]	
R13	$Hg^{2+} \rightarrow DMHg$	double methylation	4.63E-10 [s^{-1}]	Lehnherr et al., 2011
R14	$MMHg^+ \rightarrow DMHg$	bi-methylation	1.51E-08 [s^{-1}]	Lehnherr et al., 2011
R15	$DMHg \rightarrow MMHg^+$	de-methylation	2.22E-09 [s^{-1}]	Mason, 1995; Mason, 1999
R16	$MMHg^+ \rightarrow Hg^{2+}$	de-methylation	6.94E-07 [s^{-1}]	Monperuss et al., 2007
R17	$DMHg + phot \rightarrow MMHg^+$	photo de-methylation[3]	4.57E-09 [m^2 W-1 s^{-1}]	Lehnherr et al., 2007
R18	$DMHg + phot \rightarrow Hg^{2+}$	photo de-methylation[3]	4.57E-09 [m^2 W-1 s^{-1}]	Lehnherr et al., 2007
R19	$MMHg^+ + phot \rightarrow Hg^{2+}$	photo de-methylation[3]	4.57E-09 [m^2 W-1 s^{-1}]	Lehnherr et al., 2007
R20	$MMHg^+ \rightarrow Hg^0$	reductive de-methylation	2.22E-09 [s^{-1}]	Mason, 1995; Mason, 1999

Table 3: Chemical reactions as implemented in the MERCY model. (pseudo 1st order reaction rates $k_2 = k_1 C$ *depend on following variables C: [1]temperature dependent reaction rate, [2]cyanobacteria concentration dependent reaction rate, [3] photolytically active radiation dependent raction rate, [4]sulphate concentration dependent reaction rate, [5]oxygen dependent concentration reaction rate.)*

Red-ox reactions

Hg red-ox chemistry is implemented with five reactions. Reduction ($Hg^{2+} \rightarrow Hg^0$) is driven by three processes: (R1) a continuously ongoing chemical reduction, often referred to as dark reduction, (R2) photolytic reduction, and (R3) biogenic reduction (Table 3). We use reaction rates reported by Kuss et al. (2015). This leads to each reduction reaction roughly being of similar importance for the total Hg^0 production, albeit with specific distinct seasonality (note that the biogenic reduction only plays a role in the Baltic Sea due to cyanobacteria). This is in contrast to other published reaction rates where photolysis is the dominant pathway (Qureshi et al., 2009). We do not use an intermediate oxidation product (Hg^*) as we found the species to be too short-lived for the given model setup. We chose the values from Kuss (2015) as contrary to other studies as these were measured under in situ conditions. The oxidation is driven mainly by chemical oxidation (R4) while photolytic oxidation (R5) rates are much smaller leading to a net photolytic reduction. The photolysis rates are parameterized to the photolytically active radiation based on observations. The biogenic reduction reaction rate is scaled by the cyanobacteria biomass and is not triggered by other phytoplankton species (Kuss et al., 2015). For the chemical reduction, we consider a temperature-dependent reaction rate k_{rd} defined as 100% at 15°C (50% at 0°C and 125% at 20°C) (Kuss et al., 2015) (Eq. 8). Finally, we consider reductive demethylation of $MeHg^+$ (R20), which is only a minor source of Hg^0 in the model.

$$k_{rd} = 2.92\text{E-}07\, e^{(0.045\ T_w)} \qquad \text{Eq. 8}$$

T_w = Water temperature [°C]

k_{rd} = dark reduction rate [s^{-1}] (R1, Table 3)

Cinnabar formation

Additionally, we implemented Hg sulphur chemistry using oxygen concentrations calculated by ECOSMO, whereas sulphur ions (S^{2-}) are represented by negative oxygen concentrations in order to reduce the amount of transported state variables (Table 1) (Neumann, 2000). In anoxic waters cinnabar (HgS) is formed by reaction with sulphide species (H_2S, HS^-, S^{2-}) (R6, Table 3). This reaction is kinetically fast and scavenges the majority of the inorganic $Hg^{2+}_{(aq)}$ within a few hours. The product of this reaction is considered particulate but without a sinking velocity due to the small size of these particles (Paquette and Helz, 1995, Soerensen et al., 2018). In a slower reaction (R7) HgS is subsequently binding to -SH groups of DOM, a reaction that can lead to the dissolution of 50% of the HgS within 24 hours. After one day, the dissolution reaction is in equilibrium with the re-crystallisation reaction (R8). In the presence of oxygen, sulphur is quickly oxidized and HgS is readily transformed back into soluble $Hg^{2+}_{(aq)}$ species ($HgS_{(s)} + 2O_2 \rightarrow HgSO_{4\,(aq)}$) (R9). In the model, $HgSO_4$ is attributed back to the dissolved $Hg^{2+}_{(aq)}$ pool and not tracked by an additional state variable.

Organic chemistry

The organic chemistry doubles the number of variables introduced for the inorganic Hg chemistry mechanism (Figure 1). In the model, we implemented three sources for $MMHg^+$, (1) methylation in anoxic waters (R10), (2) methylation in oxic waters (R11), and (3) methylation due to biologic activity (R12). The anoxic methylation is thought to be due to anaerobic bacteria and is in our model the fastest methylation process (4.4E-07 s^{-1}). Studies have found that methylation also occurs in oxic waters although at much slower rates (Lehnherr, 2014; Heimbürger et al., 2015; Bowman et al., 2020; Soerensen et al. 2018). We implemented an additional constant methylation reaction (3.47E-08 s^{-1}) and a biologically induced methylation in oxic water to reflect the fact that numerous bacteria have been shown to actively methylate Hg (Soerensen et al., 2018; Capo et al., 2020). We use the amount of remineralized organic material as a proxy for anoxic micro environments in the oxic water column. The remineralization is dependent on temperature (Eq. 9) with DOM being mineralized at a higher rate of $k_{\mathrm{rem_{DOM}}} = 10\, k_{\mathrm{rem_{POM}}}$. Following equation 7 we calculate the amount of remineralized organic matter and use this to scale the biologic methylation rate (R12). The reaction rate R12 has been chosen such that the effective biological methylation rate mostly lies between R10 and R11 ranging from zero to 1.13E-07 s^{-1} .

$$k_{\mathrm{rem_{POM}}} = 0.006\left\{\left(1 + 20^{\left(\frac{T_w^2}{13^2 + T_w^2}\right)}\right)\right\} \qquad \text{Eq. 9}$$

$k_{\mathrm{rem_{POM}}}$ = POC reminerlization rate [day^{-1}]

T_w = water temperature [°C]

Besides $MMHg^+$ we also consider double methylation reactions producing DMHg (R 13,14). For the degradation DMHg → $MMHg^+$ → Hg^{2+}, we consider constant demethylation reactions (R15,16), photolytic degradation (R17-19), and reductive demethylation (R20). Finally, we apply methylation and de-methylation only to dissolved $Hg^{2+}_{(aq)}$ and $MeHg^+_{(aq)}$ species. Thus, high loads of DOM and POM influence the effective net methylation and produce a non-linear behaviour in the system (Olsen et al., 2018).

Chemical reactions in the sediment

In the sediments, we consider only two species: $Hg^{2+}_{(S)}$ and $MMHg^{+}_{(s)}$. These undergo methylation and demethylation using the same reactions and rates as in the pelagic zone (Table 3). We consider the sediments to always be at least partially anoxic depending on the oxygen concentration in the adjacent water layer (50 – 100% anoxic for O_2 between 2 and 0 ml/l). All abiotic methylation reactions (R10 and R11, Table 3) thus take place in the model sediment. Additionally, $Hg^{2+}_{(s)}$ is subject to dark reduction and subsequently released from the sediment as Hg^0 (Capo et al., 2022).

2.3.2 Partitioning

The speciation of Hg^{2+} and $MMHg^{+}$ plays a major role in transport, chemical reactions, and bio-availability. In the partitioning scheme we distinguish between three phases: (1) dissolved $Hg^{2+}_{(aq)}$ and $MeHg^{+}_{(aq)}$ which are stored in two advected state variables. They are further resolved into $Hg(OH)_{2(aq)}$, $HgOHCl_{(aq)}$, $HgCl_{2(aq)}$, $MeHgOH_{(aq)}$, $MeHgCl_{(aq)}$ which are diagnostic variables dependent on salinity. (2) Hg bound to dissolved organic material Hg^{2+}-$DOM_{(aq)}$ and $MeHg^{+}$-$DOM_{(aq)}$, and (3) the particulate Hg species Hg^{2+}-$POC_{(s)}$ and $MeHg^{+}$-$POC_{(s)}$.

Three-way partitioning is calculated as a function of Hg concentration, particle load, and dissolved organic matter concentration (Eqs. 10-12). As we could not obtain sorption and desorption rates and because our carbon representation does not capture the amount of O- and S- binding sites available for Hg we implemented partitioning based on partitioning coefficients instead of a dynamic sorption/desorption process as described in Eqs. 4. We use a value of $\log(k_d) = 6.6$ for Hg^{2+} associated with DOC based on the work of Tesan et al. (2020). This K_d is higher than what is used in other models (Zhang et al., 2019; Kawai et al., 2020). Moreover, we use distinct partitioning coefficients for binding to POC k_d and DOC k_l for inorganic Hg^{2+} ($\log(k_d)$ = 6.4 and $\log(k_l)$ = 6.6) and organic $MMHg^{+}$ ($\log(k_d)$ = 5.9 and $\log(k_l)$ = 6.0) (Allison and Allison, 2005; Batrakova et al., 2014) (Table 4).

$$k_d = \frac{Hg_{POC}}{POC\, Hg^{2+}_{aq}} \quad \text{Eq. 10a} \qquad k_l = \frac{Hg_{DOC}}{DOC\, Hg^{2+}_{aq}} \quad \text{Eq. 10b}$$

$$Hg_{DOC} = \frac{Hg_T\, k_d}{1 + k_d + k_l} \quad \text{Eq. 11a} \qquad Hg_{DOC} = \frac{Hg_T\, k_d}{1 + k_d + k_l} \quad \text{Eq. 11b} \qquad Hg_{POC} = \frac{Hg_T\, k_l}{1 + k_d + k_l} \quad \text{Eq. 11c}$$

k_d = Hg-$POM_{(s)}$/$Hg_{(aq)}$ partitioning coefficient [1]

k_l = Hg-$DOM_{(aq)}$/$Hg_{(aq)}$ partitioning coefficient [1]

POM = particulate organic matter [1]

SPM = suspended particles [1]

DOM = dissolved organic matter [1]

SPM = suspended particles [1]

DOM = dissolved organic matter [1]

The model assumes instantaneous equilibrium and redistributes Hg^{2+} and $MeHg^{+}$ between the three states on each time step. This approach is supported by lab studies that indicate the partitioning equilibrium is reached within an hour (Mason et al. 1994). Finally, mass conservation is ensured by Equation 12.

$$Hg_T = Hg_{aq} + Hg_{POC} + Hg_{DOC} \quad \text{Eq. 12}$$

#	Name	Description	Value	Unit	Source
1	R2P	Conversion factor short wave radiation to PAR	0.5211	unitless	Jacovides et al., 2004
2	E2W	Conversion factor Einstein to Watt	4.57	[][1]	McCree et al., 1972
3	PSR	Conversion factor POC to total particles	0.1	unitless	Sharif et al., 2014
4	F_{red}	Reducible fraction of dissolved Hg^{2+}	0.4	unitless	Mason et al., 1995; Kuss et al., 2015
5	v_{down}	Particle settling velocity	5.0	m/s	Daewel and Schrum, 2013
6	v_{up}	Upwelling velocity of cyanobacteria	0.1	day^{-1}	Daewel and Schrum, 2013
7	r_{bur}	Burial rate	0.00001	day^{-1}	Daewel and Schrum, 2013
8	v_{crit}	Critical velocity triggering resuspention	0.01	m/s	Daewel and Schrum, 2013
9	r_{res}	Resuspention rate	25	day^{-1}	Daewel and Schrum, 2013
10	FRR	Remineralization fraction DOM/POC	0.4	unitless	Daewel and Schrum, 2013
11	p_{HgCl2}	Permeability of $HgCl_2$	7.2E06	m/s	Mason et al., 1996
12	$p_{CH3HgCl}$	Permeability of CH_3HgCl	7.4E06	m/s	Mason et al., 1996
13	$\log(kd_0)$	Partitioning coefficient of Hg^{2+}	6.4	l/kg	Tesan et al., 2020 Allison and Allison, 2005
14	$\log(kl_0)$	Partitioning coefficient of Hg^{2+}	6.6	l/kg	
15	$\log(kd_0)$	Partitioning coefficient of $MeHg^{+}$	5.9	l/kg	
16	$\log(kl_0)$	Partitioning coefficient of $MeHg^{+}$	6.0	l/kg	
17	E_{H2O}	PAR extinction coefficient in water	0.05	m^{-1}	Daewel and Schrum, 2013
18	E_{phy}	PAR extinction coefficient of phytoplankton	3.77E-04	m^2/mgC	Daewel and Schrum, 2013
19	E_{DOC}	PAR extinction coefficient of DOC	2.90E-04	m^2/mgC	Daewel and Schrum, 2013
20	E_{POC}	PAR extinction coefficient of POC	2.0E-04	m^2/mgC	Daewel and Schrum, 2013

Table 4: Physical and biological constants used in MERCY v2.0.

2.3.3 Radiation

The radiation available for photolytic reactions is determined from hourly input fields using short wave radiation reaching the surface as modelled by the meteorological model COSMO-CLM (Table 1). As the reaction rates for Hg photolysis are usually reported in relation to photolytically active radiation PAR, we convert the modelled shortwave radiation using an average factor of 0.5211 not taking into account diurnal variations (Jacovides et al., 2004). We then calculate the cumulative light extinction E_{tot} (Eq. 13) by water (Eq. 14), phytoplankton (Eq. 15), dissolved organic matter (Eq. 16), and suspended particles SPM (Eq. 17). Whereby we estimate the total particulate matter concentration for light attenuation using a constant ratio of 0.1 times the particulate organic carbon POC concentration (Sharif et al., 2014) (Eq. 18). Finally, the remaining radiation R_z at half the depth of each layer is calculated following the Lambert-Beer Law (Eq. 19). All parameters used to calculate light extinction are given in Table 4.

$$E_{tot} = E_{phy} + E_{POC} + E_{DOC} + E_{water} \quad \text{Eq. 13}$$

$$E_{H2O} = \sum_{z=0}^{n} 0.05\left(h_{z+1} - h_z\right) \quad \text{Eq. 14}$$

$$E_{phy} = \sum_{z=0}^{n} 0.000377\left(C_{FLA} + C_{DIA} + C_{CYA}\right)\left(h_{z+1} - h_z\right) \quad \text{Eq. 15}$$

$$E_{\mathrm{DOC}} = \sum_{z=0}^{n} 0.00029\, C_{\mathrm{DOC}}\left(h_{z+1} - h_z\right) \quad \text{Eq. 16}$$

$$E_{\mathrm{POC}} = \sum_{z=0}^{n} \frac{0.0002 C_{\mathrm{POC}}}{\mathrm{PSR}} \left(h_{z+1} - h_z\right) \quad \text{Eq. 17}$$

$$C_{P_{\mathrm{total}}} = \mathrm{C_{POC}} / \mathrm{PSR} \quad \text{Eq. 18}$$

$$R_{z+1} = \mathrm{R}_z \exp^{(-E_z)} \quad \text{Eq. 19}$$

C_{FLA} = Flagellate concentration	[mgC/m³]	
C_{DIA} = Diatome concentration	[mgC/m³]	
C_{CYA} = Cyanobacteria concentration	[mgC/m³]	
C_{DOC} = Dissolved organic carbon	[mgC/m³]	
C_{POC} = Particulate organic carbon	[mgC/m³]	
$C_{P\ total}$ = Total particle load	[mgC/m³]	
PSR = Fraction of POC to total particles	[1] = 0.1 (Sharif et al., 2014)	
E_{phy} = Extinction by phytoplankton	[1]	
E_{DOC} = Extinction by DOC	[1]	
E_{POC} = Extinction by POC	[1]	
E_{H2O} = Extinction by water	[1]	
E_{tot} = Total light extiction	[1]	
z = number of vertical layer	[1]	
n = number of layers	[1]	
h = height of grid cell z	[m]	
R = Radiation at layer z+1	[W/m²]	

2.3.4 Biological uptake

Hg bioaccumulation has been implemented directly into the HAMSOM-ECOSMO framework (Daewel and Schrum, 2013; Daewel et al., 2019). ECOSMO is based on a functional group approach lumping species based on properties like nutrient requirements (NO_3^-, NH_4^+, PO_4^{3+}, SiO_2) and feeding habits (herbivorous, omnivorous, carnivorous). ECOSMO includes 3 phytoplankton species (flagellates, diatoms, and cyanobacteria), 2 zooplankton species (micro- and mesozooplankton), as well as a macrobenthos and a fish group with the latter representing mass fluxes to higher trophic levels (Figure 2).

In MERCY we consider bioaccumulation of inorganic Hg^{2+} and organic $MeHg^+$, for each of the 7 functional groups. Moreover, we distinguish between passive uptake directly from the water column (bio-concentration) and active uptake due to the consumption of contaminated food (bio-magnification). The first is accumulated as Hg attached to the organism (zooplankton carapace, fish gills) and the second incorporated internally. Figure 3 depicts a schematic overview of the rate constants used to describe bioaccumulation in MERCY with phytoplankton, which only undergoes passive uptake, on the left and higher trophic species, which also actively feed on other species, in the middle and on the right. All bioaccumulation processes are calculated separately for inorganic Hg^{2+} and organic $MeHg^+$ and the accumulated Hg is transported consistently with the movement of the associated biota. In total, this leads to 22 bio-accumulation state variables (6 phytoplankton, 8 zooplankton, 4 macrobenthos, and 4 fish) which roughly doubles the number of chemical state variables (20) in the model (Table 2). All parameters used for bioaccumulation modelling are given in Table 5.

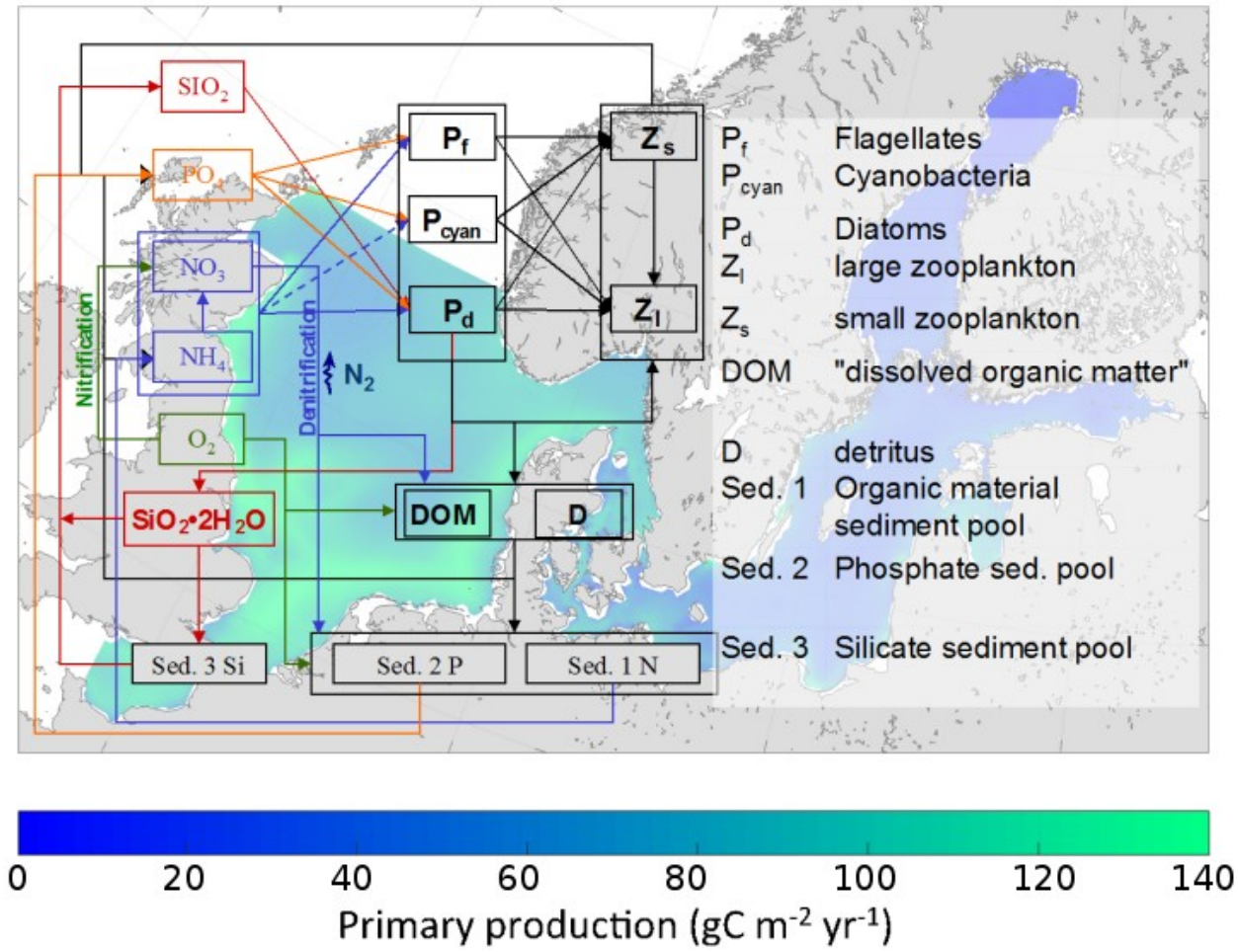

Figure 2: *Overview of the ECOSMO marine ecosystem nutrient and functional group model (Daewel et al., 2019).*

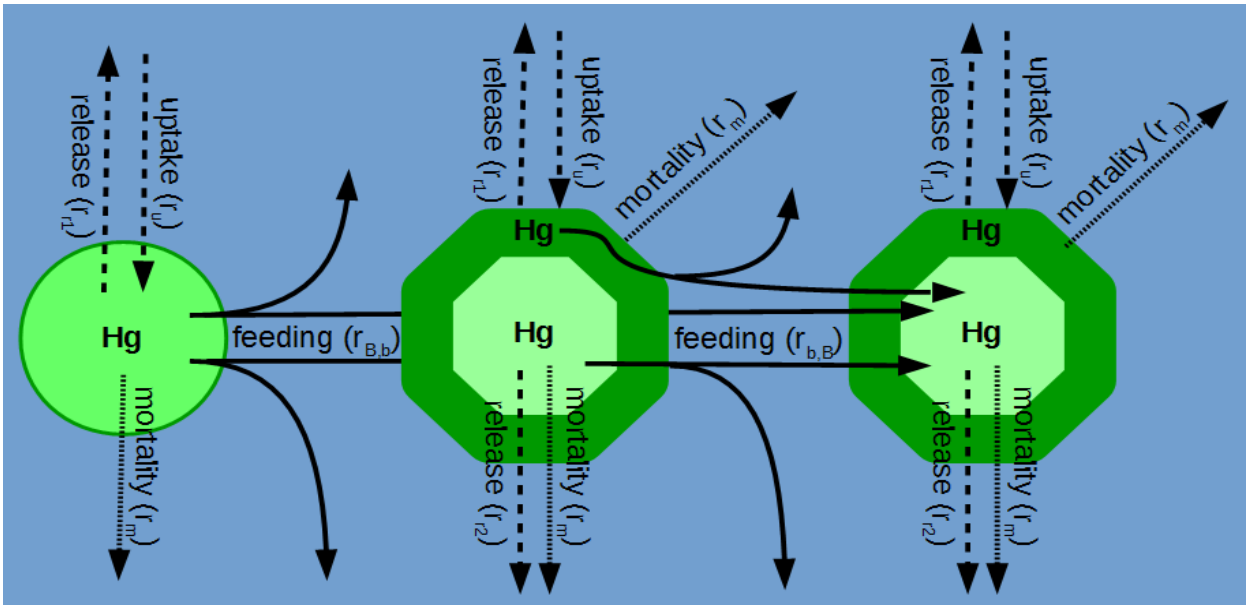

Figure 3: Schematic overview of Hg^{2+} and $MMHg^{+}$ bioaccumulation for phytoplankton (left), microzooplankton (middle), and mesozooplankton (right). Dashed lines indicate passive uptake and release rates (Eq. 19), solid lines indicate active uptake due to feeding with a fraction beeing instantly released back into the water column (Eq. 22), and dotted lines show Hg loss due to mortality (Eq. 23).

Bio-concentration

In MERCY dissolved Hg^{2+}_{aq} and $MMHg^{+}_{aq}$ are accumulated via passive uptake U_P (Eq. 20) through the cell membrane of the phytoplankton functional groups (diatoms, flagellates, cyanobacteria). For zooplankton, macrobenthos, and fish, the passive uptake is thought to lead to Hg accumulation on the surface or areas that are exposed to water like the mouth or gills in the case of fish (Figure 3: r_u). The uptake rate is r_u calculated based on an ecosystem functional group B dependent surface area $A_{(B)}$ and a Hg species dependent permeation velocity v (Eq. 21). We estimate average volume and surface areas for phytoplankton species based on observations of size and geometric shape (Table S1) (Olenina et al., 2003). The cell volume is used to estimate the organic carbon content, which is then used to estimate the organic carbon to cell surface ratio (Menden-Deur and Lessard, 2000). This ratio allows us to model the total phytoplankton cell surface per functional group based on the organic carbon content as modelled in ECOSMO. The estimated surface area is used to calculate the Hg species-dependent uptake rate based on Mason et al. (1996). Diffusive uptake by zooplankton is implemented based on experimental uptake studies but is less important compared to phytoplankton due to the comparably low surface areas of these species (Tsui and Wang, 2004).

$$U_{P(B)} = r_u \, Hg^{2+}_{(aq)} \qquad \text{Eq. 20}$$

$U_{P(B)}$ = passive uptake of ecosystem group B	[ng/s]
r_u = passive uptake rate	[s^{-1}]
$Hg^{2+}_{(aq)}$ = dissolved Hg	[ng/m^3]

$$r_u = v_C \, A_B C_B \qquad \text{Eq. 21}$$

v_i = permeation velocity for Hg species i	[m/s]
A_B = average surface area of ecosystem group B	[m^2/mgC]
C_B = concentration of ecosystem group B	[mgC/m^3]

Bio-magnification

For all non-phytoplankton species, we consider the active uptake U_A due to feeding rates $r_{B,b}$ and $r_{b,B}$ which lead to a fraction $\epsilon_{(C)}$ of the Hg in prey to be incorporated into the predator (Figure 3: $r_{B,b}$ $r_{b,B}$). Through this process, Hg^{2+} and $MMHg^{+}$ are magnified along the food web (Eq. 22). Zooplankton is feeding on detritus, phytoplankton and other zooplankton while fish feed on mesozooplankton and macrobenthos following Daewel et al. (2019) (Figure 4). Moreover, there is macro benthos that exists only in the marine bottom layer and is feeding on these species. We base our uptake on studies that show that only a fraction of Hg^{2+} ($\epsilon_{(Hg)}$ = 0.45) and $MMHg^{+}$ ($\epsilon_{(MeHg)}$ = 0.97) are incorporated into the predator, while the rest is excreted directly back into the water column (Mason et al., 1996;, Wang and Wong, 2003;, Tsui and Wang, 2004; Pickhardt et al., 2006).

$$U_{A(B)} = \sum_{b=0}^{m} r_{(B,b)} \epsilon_{(C)} Hg_{(b)} - r_{(b,B)} Hg_{(B)} \qquad \text{Eq. 22}$$

$U_{A(B)}$ = actuve uptake rate in ecosystem group B	[ng/s]
Hg_B = Hg concentration in ecosystem group B	[ng/m^3]
Hg_b = Hg concentration in ecosystem group b	[ng/m^3]
m = number of ecosystem groups	[1]
$r_{B,b}$ = feeding rate	[m^3/s]
$r_{B,b}$ = predation rate	[m^3/s]
ϵ_C = feeding efficiency	[dimensionless between 0-1]

Release

Mercury accumulated by active U_P and passive uptake U_A can also be released back into the water column (Eq. 23). There are three distinct processes in the bioaccumulation model that release Hg accumulated in the food web back into the water column. Firstly, there are species-dependent fixed release rates for Hg inside r_{r2} and on r_{r1} the biological species (Eq. 24). Secondly, upon feeding described by feeding rates $r_{\mathrm{B,b}}$ and $r_{\mathrm{b,B}}$, a fraction $1-\epsilon_{(C)}$ of the Hg accumulated in prey is not incorporated into the predator and this is directly released back into the water column (Eq. 25). Finally, based on the ECOSMO mortality and respiration rates r_m for each ecosystem group, Hg is released (Eq. 26). Feeding, mortality and respiration rates are directly taken from ECOSMO (Table 1) and the relevant equations ar described in detail in Daewel (2019). For detritus, the mortality rate is a temperature-dependent remineralization rate (Eq. 9).

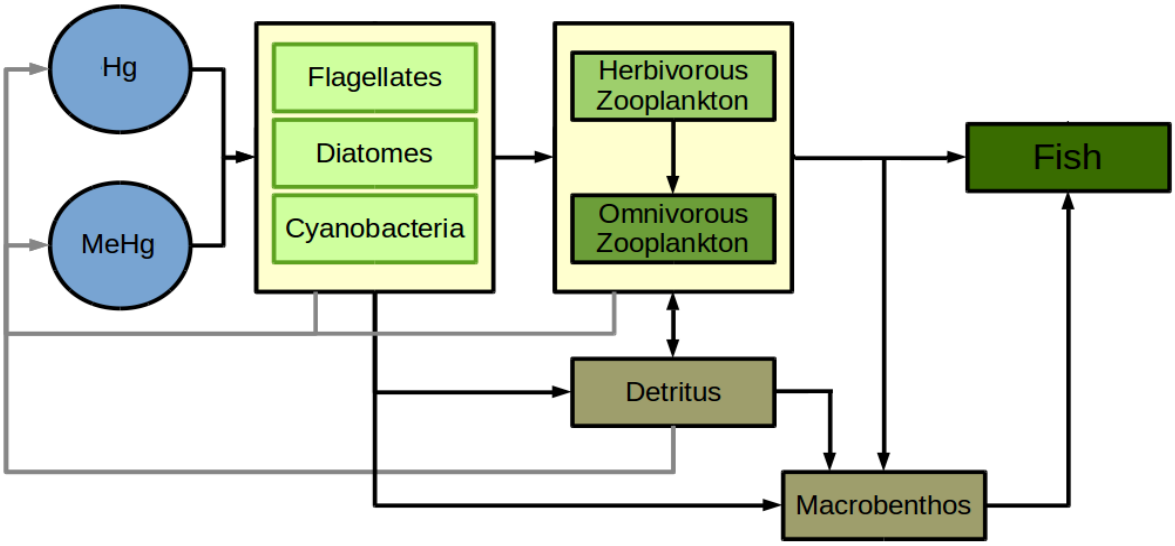

Figure 4: Flowchart of Hg bio-accumulation due to feeding following the ECOSMO end-to-end functional group approximation (Daewel, 2019). Rates for all depicted flows are given in Table 5.

$$R_{(B)}=\mathrm{R}_{\mathrm{F}(B)}+\mathrm{R}_{\mathrm{R}(B)}+\mathrm{R}_{\mathrm{M}(B)} \qquad \text{Eq. 23}$$

$\mathrm{R}_{(B)}$ = release rate from ecosystem group B [ng/s]

$\mathrm{R}_{\mathrm{R}\,(B)}$ = constant release rate [ng/s]

$\mathrm{R}_{\mathrm{F}\,(B)}$ = feeding related release rate [ng/s]

$\mathrm{R}_{\mathrm{M}\,(B)}$ = mortality related release rate [ng/s]

$$R_{\mathrm{F}(B)}=\sum_{\mathrm{B}=0}^{m}\{\sum_{\mathrm{b}=0}^{m} r_{(\mathrm{B,b})}[(1-\epsilon_{(C)\mathrm{ext}})\mathrm{Hg}_{(b)\mathrm{ext}}+(1-\epsilon_{(C)\mathrm{int}})\mathrm{Hg}_{(b)\mathrm{int}}]\} \qquad \text{Eq. 24}$$

$\mathrm{r}_{\mathrm{B,b}}$ = feeding rate of group B on group b [s^{-1}]

$\epsilon_{\mathrm{C\,int}}$ = feeding efficiency for external Hg species C [dimensionless between 0-1]

$\epsilon_{\mathrm{C\,ext}}$ = feeding efficiency for external Hg species C [dimensionless between 0-1]

$\mathrm{Hg}_{(\mathrm{b})\,\mathrm{ext}}$ = Hg on ecosystem group b [ng/m³]

$\mathrm{Hg}_{(\mathrm{b})\,\mathrm{int}}$ = Hg inside ecosystem group b [ng/m³]

$$R_{R(B)} = \sum_{B=0}^{m} r_{r1(B)} Hg_{(B)ext} + r_{r2(B)} Hg_{(B)int} \quad \text{Eq. 25}$$

$Hg_{(b)\,ext}$ = Hg on ecosystem group B [ng/m³]

$Hg_{(b)\,int}$ = Hg inside ecosystem group B [ng/m³]

r_{r1} = release rate of external Hg [m³/s]

r_{r2} = release rate of internal Hg [m³/s]

$$R_{M(B)} = \sum_{B=0}^{m} r_{m(B)} \left(Hg_{(B)ext} + Hg_{(B)int} \right) \quad \text{Eq. 26}$$

r_m = mortality rate of ecosystem group B [m³/s]

Nr	ecosystem group	Hg species	parameter	Description	value	unit	Source
1	diatoms	Hg^{2+}	r_u	uptake rate	3.95E-08	s^{-1}	*A*
2			r_r	release rate	6.58E-04	s^{-1}	*A+B*
3		$MeHg^{+}$	r_u	uptake rate	4.84E-08	s^{-1}	*A*
4			r_r	release rate	8.40E-06	s^{-1}	*A+B*
5	flagellates	Hg^{2+}	r_u	uptake rate	1.87E-08	s^{-1}	*A*
6			r_r	release rate	3.11E-04	s^{-1}	*A+B*
7		$MeHg^{+}$	r_u	uptake rate	1.82E-08	s^{-1}	*A*
8			r_r	release rate	8.40E-06	s^{-1}	*A+B*
9	cyanobacteria	Hg^{2+}	r_u	uptake rate	4.46E-08	s^{-1}	*A*
10			r_r	release rate	7.43E-04	s^{-1}	*A+B*
11		$MeHg^{+}$	r_u	uptake rate	4.34E-08	s^{-1}	*A*
12			r_r	release rate	8.40E-06	s^{-1}	*A+B*
13	zooplankton	Hg^{2+}	r_u	uptake rate	1.94E-10	s^{-1}	*Tsui and Wang, 2004*
14			r_{re}	external release rate	6.94E-06	s^{-1}	*Tsui and Wang, 2004*
15			r_{ri}	internal release rate	5.79E-07	s^{-1}	*Tsui and Wang, 2004*
16		$MeHg^{+}$	r_u	uptake rate	2.56E-10	s^{-1}	*Tsui and Wang, 2004*
17			r_{re}	external release rate	2.32E-07	s^{-1}	*Tsui and Wang, 2004*
18			r_{ri}	internal release rate	5.80E-08	s^{-1}	*Tsui and Wang, 2004*
19	fish	Hg^{2+}	r_u	uptake rate	3.88E-12	s^{-1}	*Pickhardt et al, 2007*
20			r_{re}	external release rate	3.47E-07	s^{-1}	*Pickhardt et al, 2007*
21			r_{ri}	internal release rate	6.45E-07	s^{-1}	*Pickhardt et al, 2007*
22		$MeHg^{+}$	r_u	uptake rate	1.00E-11	s^{-1}	*Pickhardt et al, 2007*
23			r_{re}	external release rate	2.30E-07	s^{-1}	*Pickhardt et al, 2007*
24			r_{ri}	internal release rate	2.30E-09	s^{-1}	*Pickhardt et al, 2007*
25	default	Hg^{2+}	ε	transfer efficiency	0.45	[1]	*Pickhardt et al, 2007*
26		$MeHg^{+}$	ε	transfer efficiency	0.97	[1]	*Tsui and Wang, 2004*
27	fish	Hg^{2+}	ε	transfer efficiency	0.158	[1]	*Wang and Wong, 2003*

Table 5: Overview of bioaccumulation parameters. External variables taken from the ecosystem model ECOSMO such as mortality (r_m) and feeding rates (r_f) are given in Table 1. The abbreviated phytoplankton references are, A: "Mason et al, 1996; Menden-Deur and Lessard, 2000; Olenina et al., 2003"; and B: "Pickhardt and Fisher, 2007; Nfon et al., 2009"

2.3.5 Benthic-pelagic coupling

Following the sediment modelling concept by Daewel (2019), we implemented a simple two-layer sediment system, where the first layer interacts with the lowest water column grid cell and the second layer represents a permanent sink.

Sedimentation

Sedimentation occurs due to the settling of Hg bound to particles and detritus. The sedimentation flux F_s is calculated using a sedimentation velocity w_d of 5 m/day for Hg bound to particles (POC) (Daewel and Schrum, 2013) (Eq. 27).

$$F_s = w_d \, Hg^{2+}_{POC} \qquad \text{Eq. 27}$$

F_S = sedimentation flux		[ng/s m^{-2}]
Hg^{2+}_{POC} = particulate mercury concentration in water		[ng/m³]
w_d = sinking velocity		[m/s]

Resuspension

Re-suspension F_r is triggered by a critical ocean current velocity of U 0.01 m/s. In case a critical current velocity is reached no sedimentation takes place and a resuspension rate r_{res} of 25 [day^{-1}] is used to release $Hg^{2+}_{(s)}$ from the first sediment layer into the lowest water grid cell (Eq. 28). Depending on the depth (< 1m) of the lowest grid cell and current velocity, resuspension can also directly affect the second lowest water grid cell.

$$F_r = r_{res} \, Hg^{2+}_{S} \qquad \text{Eq. 28}$$

F_r = resuspension flux		[ng/s m^{-2}]
r_{res} = resuspension rate		[s^{-1}]
Hg^{2+}_s = mercury concentration in sediment		[ng/m²]

Burial

Hg^{2+} and $MMHg^{+}$ in the first layer are constantly transported to the second layer which represents a permanent sink in the model. The burial flux F_b is based on a constant burial rate of k_{bur} = 1.0E-04 [day^{-1}] (Eq. 29) (Table 4).

$$F_b = r_{bur} \, Hg^{2+}_{S} \qquad \text{Eq. 29}$$

F_b = burial flux		[ng/s m^{-2}]
r_{bur} = burial rate		[s^{-1}]
Hg^{2+}_s = mercury concentration in sediment		[ng/m²]

2.3.6 Air-sea exchange

Air-sea exchange of elemental Hg^0 is one of the most important processes in the global Hg cycle. Here, we use the approach of Kuss et al. (2009; 2014) which is based on the Henry's Law constant H by Andersson et al. (2008) to determine the equilibrium between Hg^0 in water $Hg^0_{(aq)}$ and air $Hg^0_{(air)}$ (Eq. 30). Next, the transfer velocity for CO_2 k_{600} is approximated using a quadratic parametrization depending on 10m wind speed U_{10} (Eq. 31). We then calculate the transfer velocity k_w for Hg^0 by scaling k_{600} using the temperature T and salinity S dependent diffusivity of Hg^0 in water (Eqs. 32 to 35) (Kuss et al., 2014). The actual inter-compartmental Hg^0 flux F_{Hg} is then calculated based on surface concentrations in the adjacent compartments (Eq. 36). The air-sea exchange is also applied for DMHg. However, the CMAQ-Hg model does not consider DMHg yet. Hence, the atmosphere is only a sink for DMHg which is instantaneously transformed into Hg^{2+} (Niki et al., 1983) and it's fate is currently not explicitly resolved.

Eq. 30 $H_{Hg} = e^{\left(\frac{-2404.3}{T} + 6.915\right)}$ Anderssen et al., 2008

Eq. 31 $k_{600} = 0.222\,U_{10}^2 0.333\,U_{10}$ Nightinggale et al., 2000

Eq. 32 $Sc_{25} = -0.0398\,T^3 + 3.3910\,T^2 - 118.02T + 1948.2$ Kuss et al., 2014

Eq. 33 $Sc_0 = -0.0304\,T^3 + 2.7457\,T^2 - 118.13T + 2226.2$ Kuss et al., 2014

Eq. 34 $Sc = \frac{Sc_{35} S + Sc_0 (35 - S)}{35}$ Kuss et al., 2014

Eq. 35 $k_w = k_{600} \sqrt{\frac{Sc}{600}} / 360000$ Kuss et al., 2014

Eq. 36 $F_{Hg} = \frac{Hg^0_{(air)} - H_{Hg} * Hg^0_{(aq)}}{k_w}$ Schwarzenbach et al, 2003

H_{Hg}	= Henry's Law constant	[1]
T	= water temperature	[°C]
S	= salinity	[psu]
Sc_{35}	= Schmidt number for salt water	[1]
Sc_0	= Schmidt number for fresh water	[1]
k_{600}	= transfver velocity of CO_2	[cm/h]
k_w	= transfer velocity of Hg	[cm/h]
$Hg^0_{(air)}$	= Hg^0 concentration in air	[ng/m³]
$Hg^0_{(aq)}$	= Hg^0 concentration in water	[ng/m³]
F_{Hg}	= net Hg^0 flux from atmosphere to water	[ng m^{-2} h^{-1}]

2.3.7 Technical implementation

As basis for the presented model development we build upon the setup used for the earlier published inorganic marine Hg model MERCY (Bieser and Schrum, 2016). All processes are implemented as stand-alone routines which are called from a main driver function containing several time loops (Figure 5). Data for the wet cells (pelagic) are stored in vector form to overhead and data for sediments (benthic) and the lowest atmospheric layer are stored in 2d fields. Input data (Table 1) is read directly during run time from binary ECOSMO output as hourly mean values. This approach was chosen because there is no feedback from the Hg chemistry on the physical and biological models, and it allows us to reduce the computational costs of running the marine Hg model. All output files are created with daily mean values and saved in netCDF format using the IO-API interface (Byun and Schere, 2016; IO-API). The model is set up in a way that it runs for a single year using the last output timestep of the previous year as initial condition. For this initial model evaluation, we run MERCY for 17 years from 2000 to 2016.

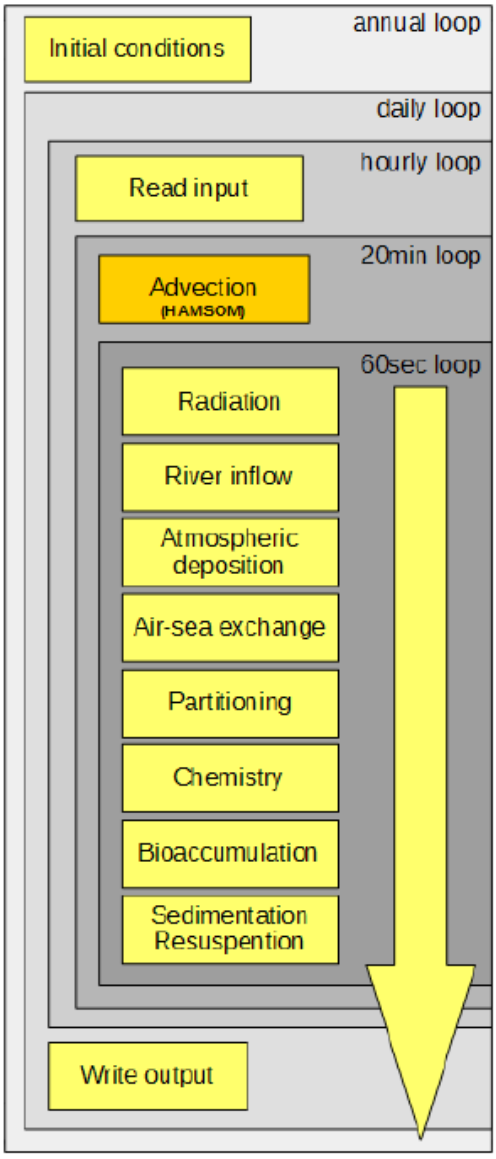

Figure 5: Schematic overview of the MERCY model routines and main time loop.

3 Model evaluation

We determine the model performance in reproducing observed concentrations and dynamics (e.g. variability and seasonality) of individual Hg species. Based on this analysis we identify the processes and parameters responsible for the model error. The model is not specifically calibrated to the area of application, the North and Baltic Seas. It is built on the current understanding of mercury cycling in the ocean and should be generally applicable. Major factors that need to be considered before applying the MERCY model to other regions are: (1) partitioning coefficients to organic material (OM) as the type of OM varies regionally, (2) the parametrization for biogenic reduction as the values presented here are based on cyanobacteria in the Baltic Sea, (3) the uptake and release rates for bioaccumulation which might not be representative for other regions and (4) the used ecosystem model needed to drive MERCY.

3.1 Statistics

Because there are no established quality criteria for marine models we use criteria commonly used for for evaluation of atmospheric CTMs (Derwell et al., 2010; Thunis et al., 2012; 2013; Carnevale et al., 2014). We start by comparing the observed and predicted means (Eq. 37) using daily model averages in the corresponding 10x10km² grid cell to the observation. As statistical metrics, we use bias (Eq. 38), error (Eq. 39), standard deviation (Eq. 40, 41), and correlation coefficient (Eq. 42) to evaluate systematic error, random error, amplitude error, and phase error. However, for most Hg species the observations lack the temporal coverage to determine the phase error. Moreover, we use the centered root mean squared error (CRMSE) because it allows us to distinguish between systematic error (bias) and random error (CRMSE) (Eq. 43) (Carnevale et al., 2014). For our analysis, we normalize the statistical metrics to get concentration-independent values and allow for better comparability between different Hg species.

mean: $$\mathrm{O}=\frac{1}{N}\sum_{i=0}^{N} O_i P=\frac{1}{N}\sum_{i=0}^{N} P_i \quad \text{(Eq. 37)}$$

P_i = Predicted value from the model

O_i = Observed values from measurement

N = Sample size / number of observations

i = index

normalized mean bias: $$\mathrm{NMB}=\frac{P-O}{O} \quad \text{(Eq. 38)}$$

normalized centered root mean squared error: $$\mathrm{NCRMSE}=\frac{\sqrt{\frac{1}{N}\sum_{i=0}^{N}\{(O_i-O)-(P_i-P)\}^2}}{O} \quad \text{(Eq. 39)}$$

standard deviation: $$\sigma_o=\sqrt{\frac{1}{N}(O_i-O)^2} \qquad \sigma_p=\sqrt{\frac{1}{N}(P_i-P)^2} \quad \text{(Eq. 40)}$$

normalized mean standard deviation: $$\mathrm{NMSD}=\frac{\sigma_P-\sigma_O}{\sigma_O} \quad \text{(Eq. 41)}$$

correlation correlation (r): $$\mathrm{r}=\frac{\frac{1}{N}\sum_{i=1}^{N}(O_i-O)(P_i-P)}{\sigma_O\sigma_P} \quad \text{(Eq. 42)}$$

root mean square error: $$\mathrm{RMSE}^2=\mathrm{CRMSE}^2+\mathrm{bias}^2 \quad \text{(Eq. 43)}$$

Finally, we use additional quality criteria to determine model performance. Firstly, the percentage of model values within a factor of 2 (FAC2), which gives an easy-to-understand estimate of the model quality (Eq. 44). We argue that model values within a factor of 2 are within the combined uncertainty. The uncertainty consists of the measurement uncertainty, the sampling uncertainty when comparing observations with time (24h) and space (100km²) integrated model grid cells (Schutgens et al., 2010) and the error propagation in the biogeochemical modelling framework. We estimate the measurement error U to to be in the range from 20% for Hg^0 and Hg_T and 50% for (MeHg).

Factor of 2 $$\mathrm{FAC2} = \frac{1}{N}\sum_{i=1}^{N} n_i \qquad \text{(Eq. 44)}$$

with $n_i = 1$ for $0.5 < \frac{P_i}{O_i} < 2$ and else $n_i = 0$

Secondly, we use the more technical model quality objective (MQO) as defined by Carnevale et al., (2014). The MQO (Eq. 45) relates the root mean squared error (Eq. 46) to the root mean squared uncertainty (Eq. 47). The MQO can be interpreted as follows: For $\mathrm{MQO} < 0.5$ on average the model values lie within the measurement uncertainty and thus the model cannot be improved upon unless more precise observations become available. For $\mathrm{MQO} > 1.0$ the model error is on average larger than the measurement uncertainty but the model may be closer to the 'true' environmental value than the observations. Thus, the aim is to achieve an $\mathrm{MQO} < 1.0$. Moreover, we determine model performance criteria for NMB, NMSD, and RMSE as proposed by Carnevale et al. (2010) (Eqs. 49-51).

model quality objective: $$\mathrm{MQO} = \frac{1}{2}\frac{\mathrm{RMSE}}{\mathrm{RMS}_U} \qquad \text{(Eq. 45)}$$

root mean squared error: $$\mathrm{RMSE} = \sqrt{\frac{1}{N}\sum_{i=1}^{N} (P_i - O_i)^2} \qquad \text{(Eq. 46)}$$

root mean squared uncertainty: $$\mathrm{RMS}_U = \sqrt{\frac{1}{N}\sum_{i=0}^{N} U^2} \qquad \text{(Eq. 47)}$$

U = measurement uncertainty

model performance criterion: $$MPC_{NMB} = \frac{2U}{O} \qquad \text{(Eq. 48)}$$

model performance criterion: $$MPC_{NMSC} = \frac{1}{\sigma_O}\frac{U}{} \qquad \text{(Eq. 49)}$$

model performance criterion: $$MPC_{RMSE} \leq 1.0 \qquad \text{(Eq. 50)}$$

These quality criteria have been developed for atmospheric pollutants like ozone, nitrogen oxides, and fine particles which have been studied and modelled for decades. For modelling of Hg in the marine environment, the observations are still very limited compared to that of pollutants in the atmosphere. This reflects on the ability to use these criteria and we therefore do not expect the MERCY model to meet the criteria at this point. However, we define these as our future goal for marine Hg modelling.

3.2 Model domain (North Sea and Baltic Sea)

Here, we evaluate the model for the North and Baltic Sea in northern Europe (model domain shown in Figure 6). This area was chosen for model evaluation as it covers a large range of different physical and biological conditions: The Baltic Sea (Figure 6; marine regions 8-15) is an enclosed shelf sea with a surface area of 377 000 km². It is connected to the North Sea (marine regions 1-5) via the shallow Kattegat and Skagerrak (marine regions 6-7) in the southwest. It is a brackish water body strongly influenced by freshwater inflow and it covers a salinity range from <2 PSU in the north that increases towards the southwest reaching up to 35 PSU in the transition zone between the North- and Baltic Sea. The central Baltic has several deep basins reaching a depth of 460 in the Landsort deep in the Central Baltic Sea (Figure 6b). It exhibits strong stable stratification with more saline, and in parts anoxic, deep water, resulting from an estuarine circulation system with upper layer outflow of fresh water and lower layer saline inflow. Every few years, large quantities of oxic and saline waters are transported from the North Sea to the Baltic Sea during so-called Major Baltic Inflows (MBI). During the simulation period 2000 to 2015 three MBIs occurred, one of these was an especially strong event during the winter of 2014-2015 (Fischer et al., 1996; Lehmann et al., 2015). In the northern part of the Baltic, the Bothnian Sea and the Bothnian Bay are seasonally covered by ice, possibly leading to accumulation of Hg from rivers during winter due to the suppression of Hg^0 evasion. Finally, the Baltic Sea is a system with cyanobacteria, which make it an interesting study area as they have been shown to actively reduce $Hg^{2+}_{(aq)}$ (Kuss et al., 2015). Moreover, cyanobacteria can lead to pronounced early spring / late summer biomass blooms affecting bioaccumulation (Soerensen et al., 2016).

The North Sea has a surface area of 575 000 km² and is connected to the Atlantic Ocean at its northern border and via the English Channel to the South. It is a shallow shelf ocean that is well mixed during autumn and winter and it experiences frequent resuspension events during autumn and winter storms. The southern North Sea is characterized by strong tidal mixing and thus water masses are well mixed and sediments are resuspended regularly within the tidal cycle. It is an area of high primary productivity and an important fishing ground. Thus, it is an important study area for Hg methylation and bioaccumulation.

Due to the close vicinity to the coast and national monitoring programs, there is a comparably large number of Hg observations available for both the North Sea and the Baltic Sea. However, the data on Hg are still sparse in some areas, especially regarding Hg speciation, which is a major obstacle for model evaluation.

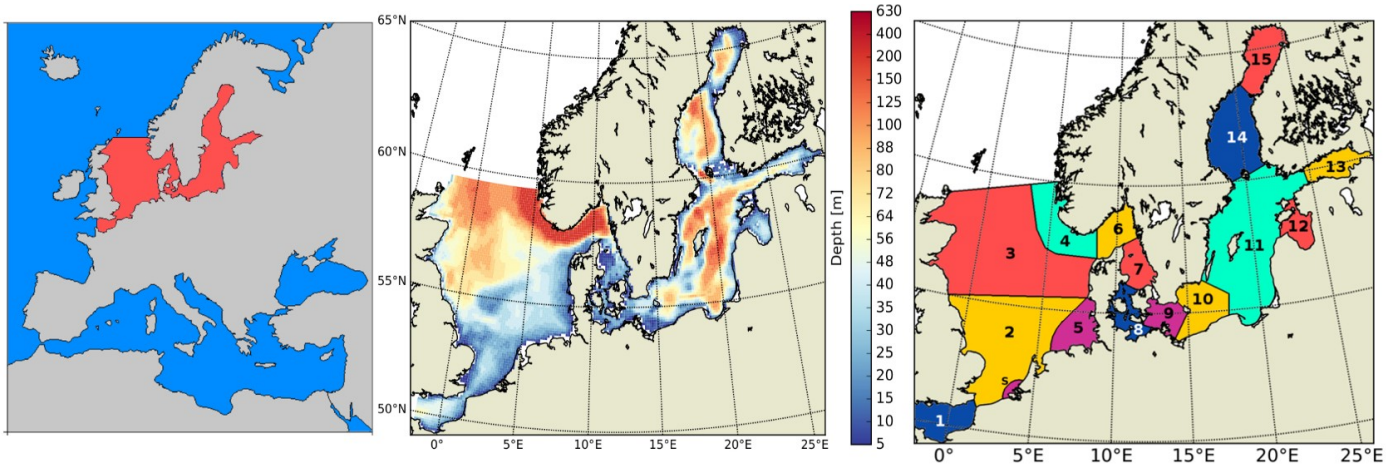

Figure 6: Left: COSMO-CMAQ-Hg atmospheric model domain with North- and Baltic Sea highlighted. Middle: MERCY marine model domain and topography. Right: Marine regions: (1) English Channel, (S) Schelde Estuary, (2) Southern North Sea, (3) Northern North Sea, (4) Norwegian Trench, (5) German Bight, (6) Kattegat, (7) Skaggerak, (8) Belt Sea, (6-8) Swedish west coast, (9) Arkona Sea, (10) Bornholm Sea, (11) Gotland Sea or Baltic Proper, (12) Bay of Riga, (13) Neva Bay, (14) Bothnian Sea, (15) Bothnian Bay.

3.2.1 Forcing data

To generate the necessary forcing data (Table 1) to run the MERCY model, we used the four models described in Section 2.1. For the atmosphere, COSMO-CLM was run on a regional domain for Europe driven by ERA interim re-analysis data (Berrisford et al., 2011). The atmospheric model domain covers the entire European land mass, including North Africa and western Russia with a resolution of 24x24km and 35 vertical layers (Fig. 6a). The calculated meteorology is then used as forcing for the atmospheric CTM CMAQ-Hg which is set up for the same domain and resolution (Buyn and Schere, 2006; Zhu et al., 2015; Bieser et al., 2016). CMAQ-Hg uses boundary concentrations for Hg by an ensemble of the global Hg models GEOSChem, GLEMOS, ECHMERIT, GEM-MACH-Hg (Travnikov et al., 2018) and all other relevant trace gases from the global CTM MOZART (Horowitz et al., 2003). Emissions for the year 2010 were created with the SMOKE-EU emission model (Bieser et al., 2011). Hg emissions are based on the AMAP emission inventory (AMAP, 2010). This is a similar setup as used in previous studies (Bieser and Schrum 2016). For computational reasons, we calculated only one year (2010) of atmospheric Hg concentration and deposition fields. These were used as boundary conditions for the marine Hg model for all years of the simulation. The ocean-ecosystem model HAMSOM-ECOSMO was run on a model domain covering the entire Baltic Sea and the North Sea with open boundaries in the English Channel and at 63° North, where the North Sea is connected to the Atlantic (Fig. 6b). The resolution of the model is about 10x10 km^2 (spherical grid) with 20 layers and a maximum water depth of 630m. The vertical resolution is 5m for the four uppermost layers with a bottom layer depth of 250m.

3.2.2 Initial conditions

As initial conditions, we interpolated observations in water, biota, and sediment using a traditional Krieging methodology to produce realistic initial starting conditions (mostly the pronounced vertical gradient) and minimize the spin-up time required (Cressie, 1990). The observational Hg data were retrieved from the database of the German Federal Maritime and Hydrographic Agency (MARENET, 2020). We run the model using initial conditions multiplied by factors of 0.5 and 2.0 and tested the time necessary for the two runs to converge. For our model domain, which is a relatively small and in parts enclosed shelf sea area, the model runs started to converge already after a few years in the water column but took several years for Hg in sediments and biota (expecially in higher trophic levels). For this study, we used a spin-up time of 30 years to reach realistic initial conditions for the production runs.

3.2.3 Boundary conditions

The chosen domain, including only the North Sea and Baltic Sea, has only a very small open boundary. The English Channel in the southwest, which forms a narrow connection to the Atlantic Ocean and the wider opening in the Northern channel. The North Sea in the north of the domain, which receives the most of the Atlantic inflow is connected to the open Atlantic Ocean at the shelf break. This region is characterized by an outflow in the eastern part and inflow in the western part. At the open boundaries, we prescribe constant Hg concentrations using 1.0 pM Hg_T for the North Atlantic and 3.0 pM Hg_T in the English Channel (Cossa et al., 2018; Leemakers et al., 2001).

3.2.4 River loads

River loads are taken from OSPAR and HELCOM reports and the Norwegian Tilførsel program (Green et a., 2011, HELCOM, 2007; 2011). We implemented rivers using monthly load data in the North Sea and annual values for the Baltic Sea as described in Bieser and Schrum (2016). The annual inflow of Hg through rivers is 1100 kg/a for the Baltic and 2800 kg/a for the North Sea. In the North Sea, the largest fluxes are from the rivers Elbe (1160 kg/a) and Rhine (800 kg/a).

3.2.5 Deposition of Hg^{2+} and atmospheric Hg^0

Dry and wet Hg deposition is read in as hourly totals from CMAQ netCDF output files. The deposited $Hg^{2+}_{(g)}$ and $Hg^{2+}_{(p)}$ is added to the dissolved $Hg^{2+}_{(aq)}$ species assuming instant dissolution of atmospheric particles. In CMAQ, the exchange of Hg^0 is set to zero for all grid cells with land use category water to avoid a doubling of the air-sea exchange calculation in the atmospheric model.

3.3 Observational data

For the model performance we start by evaluating total Hg (Hg_T) concentrations in the water column. We then look at the individual species, elemental Hg^0 and organic MeHg. Next, we evaluate the model skill in reproducing Hg concentrations in biota. For this, we compare Hg and MeHg loads in phytoplankton and zooplankton, and finally total Hg in fish (Hg_{Fish}).

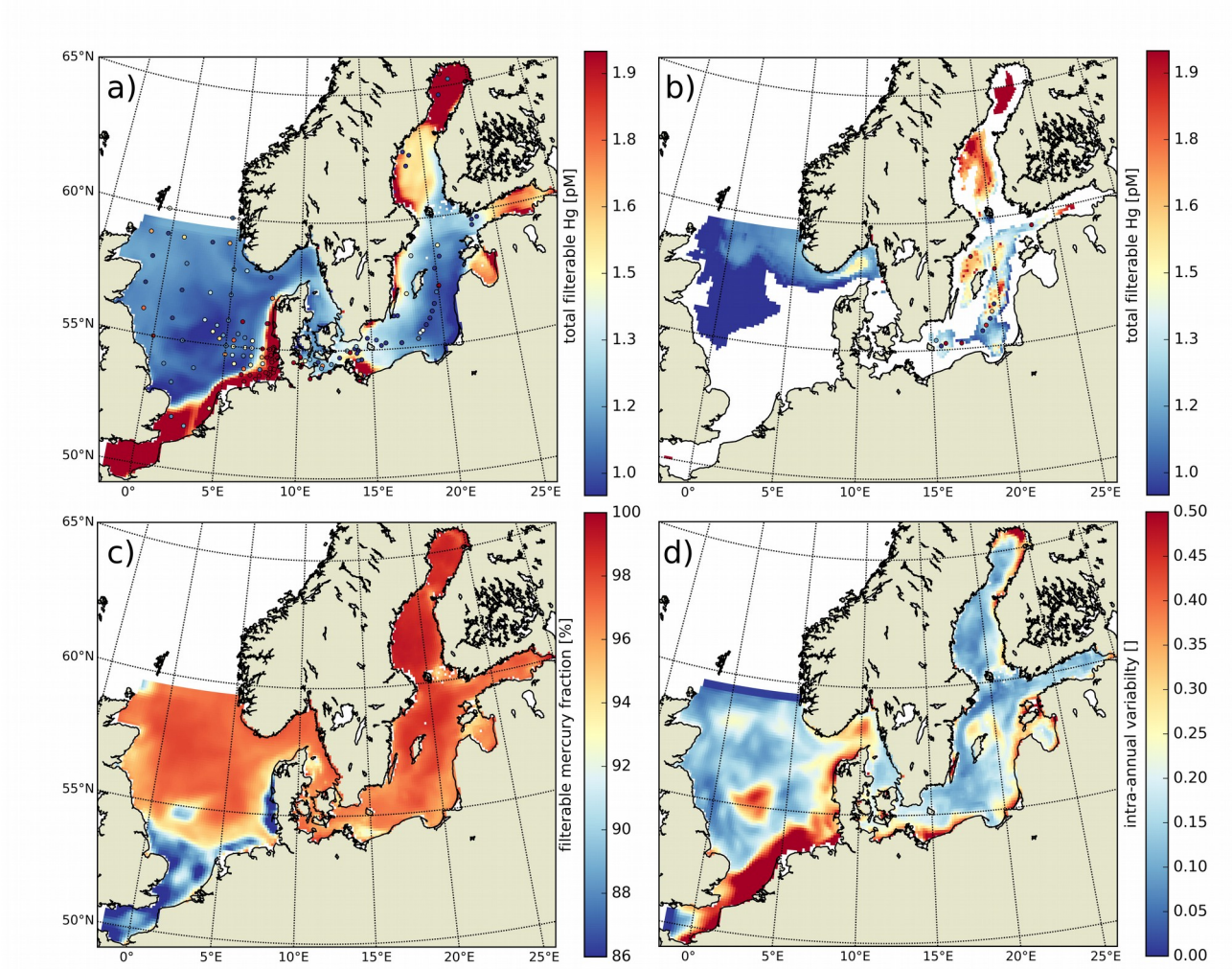

Figure 7: Annual averages: a) Hg_T concentrations in the top 50m with superimposed observations (Kuss et al., 2017; Soerensen et al. 2018; MARNET, 2020), b) Hg_T concentrations below 50m with superimposed observations, c) average fraction of filterable $Hg_{Filt.}/Hg_T$, d) intra-annual variability of modeled daily average Hg_T concentrations.

3.3.1 Total Hg in water

The available Hg_T observations cover offshore and coastal areas in the North and Baltic Sea. Hg_T has been measured as both unfiltered (Soerensen et al. 2018) and filterable fraction $Hg_{Filt.}$ (Kuss et al., 2017; MARNET, 2020). In MERCY,

$Hg_{Filt.}$ corresponds to the sum of 9 species, namely $Hg^0_{(g)}$, $Hg^{2+}_{(aq)}$, Hg-$DOM_{(aq)}$, HgS-$DOM_{(aq)}$, $MMHg^+_{(aq)}$, MMHg-$DOM_{(aq)}$, $DMHg_{(g)}$, and $HgS_{(s)}$ (Table 2). Hg_T additionally includes Hg_P, which are comprised by the two particulate species Hg-$POC_{(s)}$ and MeHg-$POC_{(s)}$. In our model $Hg_{Filt.}$ makes up about 95% of Hg_T on average (Figure 7c). Hg_P only plays a significant role (>5% on annual average) in the southern North Sea and the Wadden Sea. Especially in the Wadden Sea observed Hg_T concentrations are extremely high with values ranging from 6 to 117 pM. For the model performance evaluation, we removed measurements taken in the Wadden Sea and other areas not resolved in our model setup (e.g. the area between coast line and barrier islands and lagoons in the Baltic Sea). As depicted in Figure 7a, virtually no observations are from regions where particles play a major role. Thus, for simplification we will use the term Hg_T to refer to all of these observations, but compare them to concentrations of the respective model species.

In the North Sea we use 435 measurements of Hg_Tsampled between 2007 and 2011 (MARNET, 2020). The samples are taken over the entire year but BSH (The German Federal Maritime and Hydrographic Agency) sampling focuses mostly on the German exclusive economic zone, yet also includes a few years with data for the greater North Sea. Finally, all measurements are surface samples (0-20m) which is due to the shallow nature of the North Sea. For the Baltic Sea, there are 111 observations from the MARNET database (MARNET, 2020), 168 observations from three cruises in March 2014, March 2015, and July/August 2015 which cover the southern part of the Baltic Sea from the Belt Sea to the Gotland Deep (Kuss et al., 2017), and 90 observations from three cruises in July and August of 2015 and 2016 which in addition includes observations on the Bothnian Sea and Bothnian Bay (Soerensen et al., 2018). Figure 7a,b depict all Hg_T observations used for model evaluation.

3.3.2 Individual marine species: Hg^0 and $MMHg^+$

For the evaluation of Hg^0, we use 580 measurements from four Baltic Sea cruises in February, April, July, and November 2006 (Kuss et al., 2014). This dataset allows us to investigate the seasonality of red-ox reactions. For $MMHg^+$ we were able to obtain 310 measurements from six cruises in 2014, 2015, and 2016 covering coastal and offshore areas of the Baltic Sea (Kuss et al., 2017; Soerensen et al., 2017; 2018). For 160 of these both MeHg and Hg_T were available which enable a relative evaluation of methylated fraction M_{frac} = MeHg/HgT. For the North Sea, no Hg^0 or $MMHg^+$ observations are available at all with the exception of 9 MeHg measurements from 1999 in the English Channel and the Schelde Estuary which we used to set the $MMHg^+$ boundary conditions in the English Channel (Leemakers et al., 2001). Thus, we are forced to limit the model evaluation for Hg^0 and $MMHg^+$ to the Baltic Sea.

3.3.3 Hg in biota

Bioaccumulation in the marine biota is evaluated by comparing their total Hg and MeHg content to measured concentrations in biota in the Baltic Sea (Nfon et al, 2009). For evaluation of fish total Hg we use Hg_T concentration in muscle of 1166 herring from coastal and offshore location in the Baltic Sea (Soerensen and Faxneld, 2020). As the biota measurements are in wet weight and our model is in mg carbon dry weight, the ratio of mg carbon per mg biota of: 0.2 for diatoms, 0.33 for flagellates and cyanobacteria, and 0.5 for zooplankton and fish was assumed (Sicko-Goad et al., 1984; Walve and Larsson 1999). This was combined with a conversion factor of dry weight to wet weight of 0.2 for phytoplankton, 0.16 for zooplankton, and 0.1 for fish (Cushing 1958; Ricciardi and Bourget 1998). For phyto- and zooplankton, the model is compared to the observed average, minimum and maximum concentrations, but due to limited data no seasonal or regional comparison was possible. For fish we analyse Hg accumulation for five Baltic Sea regions ranging from the western Baltic to the Bothnian Bay.

3.4 Model performance

3.4.1 North Sea (Hg_T)

Figure 8 compares the frequency distribution of 435 Hg_T measurements to the associated model values. It can be seen that the majority of observations lie between 1 and 3 pM, which is captured well by the model. However, the observed high values between 5 and 10 pM cannot be reproduced. We argue that these are due to input from the coastal area (e.g. major rivers, Wadden Sea) not included as input to the model in the current river discharge scenario.

HgT concentrations in the North Sea do not exhibit a pronounced seasonality and the observed variability is driven by a strong land-sea gradient along the European coastline where Hg from rivers is transported north-eastwards from the English Channel by the Coriolis force (Figure 7d). For the analysis, we split the North Sea Hg observations into two groups: (1) The Elbe Estuary (N=366) and (2) the open North Sea including a few observations near the remaining coastline (N=69). Due to the significant Hg inflow from the Elbe (1164 t/a), Hg concentrations are higher in the Elbe estuary with a mean concentration of 3.44 pM (Table 6). The model is able to reproduce the observed average (NMB = -21%), but has a better agreement with the median values (-12%). In this region, random and amplitude errors are dominant. This is indicative of subgrid dynamics and our inability to resolve the seasonality of Hg from rivers stemming from the use of static river loads for the entire run (OSPAR, 2016). However, with 70% of model values within a factor of 2 of the observations and an MQO = 1.48 the model is still close to our quality goal.

In the less dynamic open North Sea, the model performs better (FAC2 = 84%, MQO = 1.22) (Table 6). The observed average of 1.92 pM is matched by the model (2.03 pM) and the bias is close to zero (NMB=6%). Nevertheless, due to the inhomogeneous distribution of observations, this value is not indicative of the actual background Hg concentrations in the open North Sea. We find, that Hg concentrations there are mostly in the range of 1.1 to 1.5 pM.

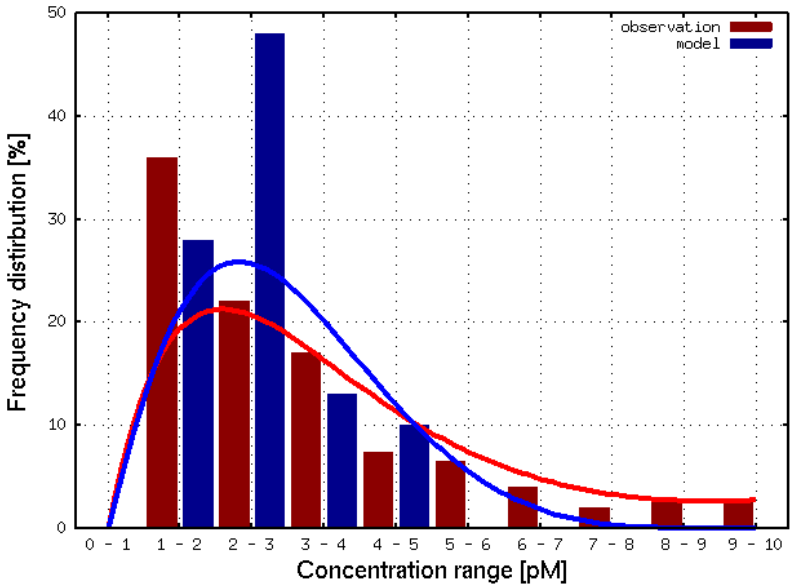

Figure 8: Frequency distribution of observed (red) and model (blue) $Hg_{Filt.}$ Concnetrations for the North Sea (N=435).

In summary, for Hg_T, the model is close to our quality criterion (MQO<=1.0). Improvements to the MQO could likely be achieved by increasing model resolution in the complex coastal regions and including more detailed input from rivers and particle resuspension at the European coastline. Especially for the Wadden Sea, a hydrodynamical model that can model the intertidal zone would be preferential.

Elbe Estuary	obs [pM]	mod [pM]	NMB	NCRMSE	FAC2	MQO	N
mean	3.44	2.71	- 0.21	0.66	70 %	1.48	366
median	2.78	2.44	- 0.12				
stdev	2.16	0.82	- 0.62				
Open North Sea	**obs [pM]**	**mod [pM]**	**NMB**	**NCRMSE**	**FAC2**	**MQO**	**N**
mean	1.92	2.03	0.06	0.69	84 %	1.22	69
median	1.68	1.74	0.03				
stdev	0.80	0.67	- 0.16				

Table 6: Regional model performance for Hg_T in the North Sea. The evaluation is based on 435 measurements from the MARENET database (MARENET, 2020).

3.4.2 Baltic Sea (Hg_T)

In the Baltic Sea, model performance for Hg_T is similar to the North Sea (FAC2 = 70%, MQO = 1.28) with a low bias (NMB = -19%) and a high random error (NCRMSE = 102%) (Table 7). Unlike for the North Sea, the model predicts a pronounced seasonality with surface Hg_T concentrations around 50% higher during March (Figure 9a) compared to August (Figure 9b) which is in line with observations from Kuss et al. (2017) taken in March and July/August (Figure 9). The two processes governing this are: (1) Stratification and particle settling in the central Baltic deep basins after the onset of primary production. This is the biological pump as POC particles here are mainly of biological origin (detritus). And (2) increased photoreduction and subsequent atmospheric exchange of Hg^0 (air-sea exchange). Additionally, during winter higher atmospheric Hg^0 concentrations due to heating related emissions and a shallow planetary boundary layer reduce and sometimes even reverse the Hg^0 air-sea gradient. In the open Baltic Sea, Hg concentrations are mostly between 1.0 and 1.5 pM. In stratified areas, Hg_T concentrations can drop down to 0.5 pM during summer. During autumn and winter mixing and upwelling can occasionally transport Hg from deeper waters upwards, sometimes leading to surface concentrations above 2 pM in some areas.

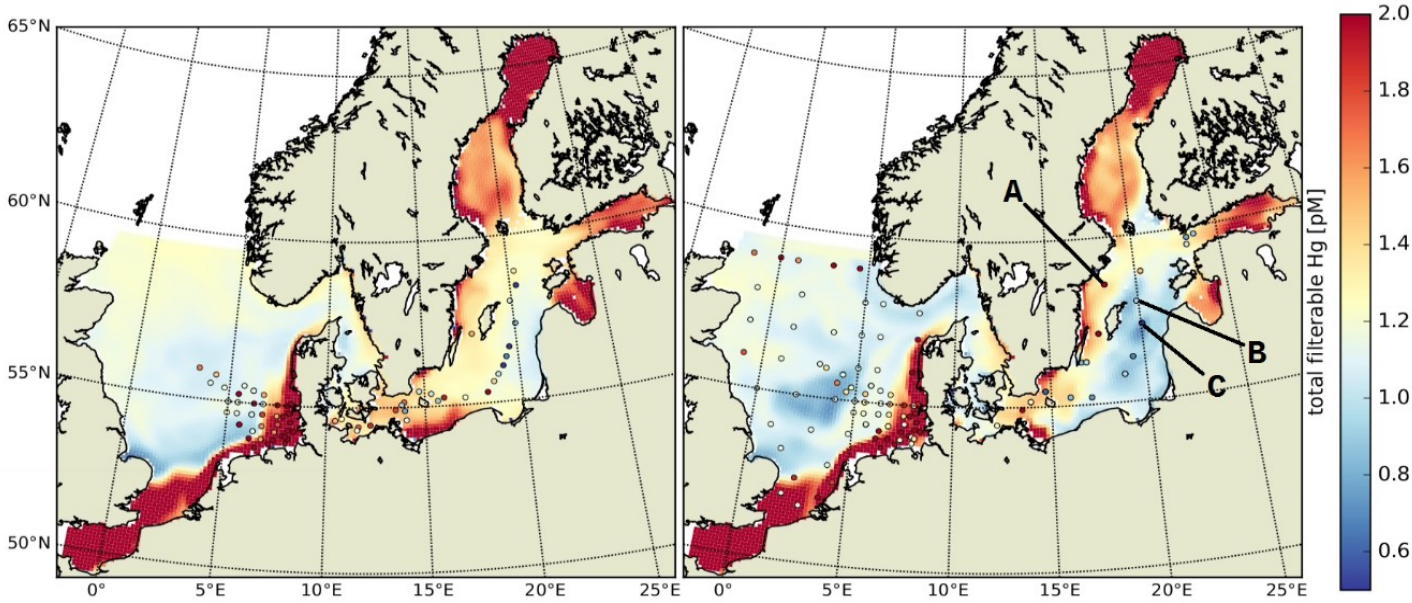

Figure 9: Hg_T surface concentrations for a) March and b) August. Dots indicate observations (Kuss et al., 2017; Soerensen et al., 2018; MARNET, 2020).

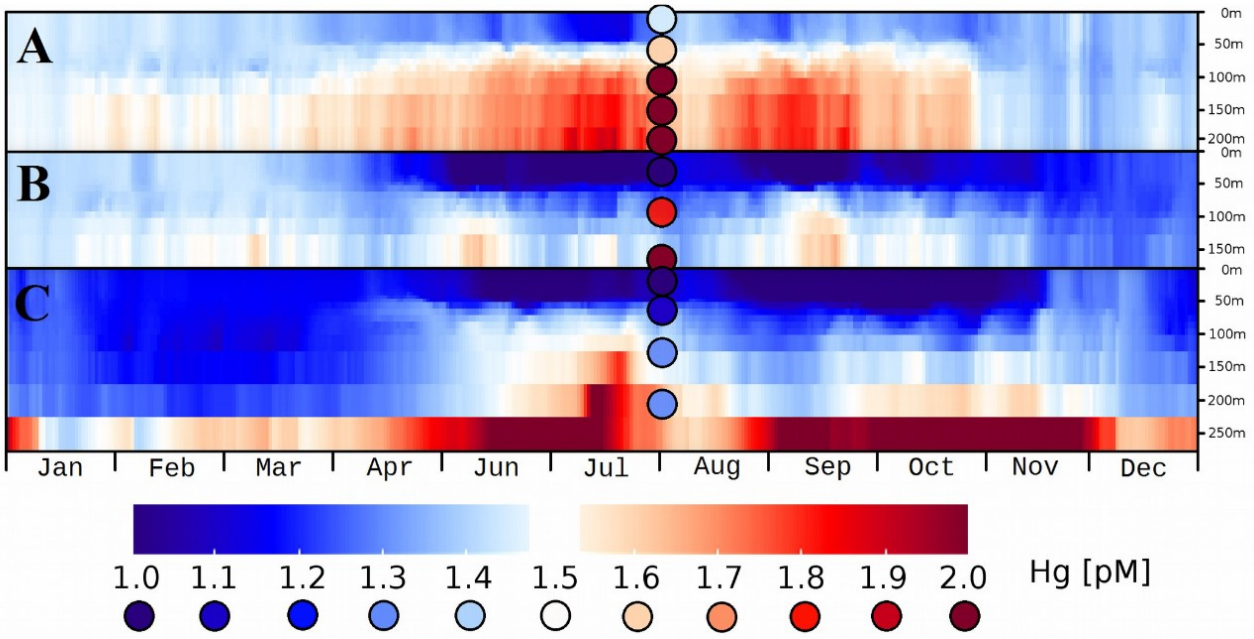

Figure 10: Surface transect of the Hg_T concentrations in the Baltic Sea. The x-axis gives 365 daily averages for the year 2010, the y-axis represents a transect from the German coast in the western Baltic (y=0) to the mouth of the Bothnian Sea (y=87).

Region	Depth	obs [pM]	mod [pM]	NMB	NCRMSE	FAC2	MQO	N
Baltic Sea (all)	**0 – 250m**	**1.83**	**1.45**	**- 0.19**	**1.02**	**70%**	**1.28**	**336**
Western Baltic	0 – 100m	1.55	1.50	- 0.03	0.97	72 %	1.76	168
Central Baltic	0 – 100m	1.39	1.39	0.00	0.81	73 %	1.03	103
Central Baltic	100 – 250m	2.38	1.51	- 0.37	0.67	67 %	1.02	50
Nothern Baltic	0 – 100m	0.85	1.82	1.16	1.25	23 %	2.01	15

Table 7: Observed and modelled seasonal and regional of $Hg_{Filt.}$ concentrations in the Baltic Sea.

For a more detailed analysis, we separated the Baltic Sea into three regions: (1) The western part, which includes the Belt, Arkona, and Bornholm Sea, (2) the Gotland Sea in the central Baltic, and (3) the northern part which includes the Bothnian Sea and Bothnian Bay. Moreover, we evaluate the oxic surface/intermediate waters and the deep anoxic waters in the Gotland area separately (Table 7). It is seen, that the model is able to reproduce surface concentrations in the western and central areas with a bias close to zero. The model bias is larger in the deep basins but model performance is still comparable to the North Sea. Here, the low vertical resolution in the model setup below 100m will play a role. In the northern part, the model strongly overestimates Hg_T concentrations. This overestimation was also seen in the Soerensen et al. (2018) model. Northern Baltic rivers tends to be low in POC but rich in DOC compared to temperate rivers (McClelland et al. 2016; Soerensen et al. 2017) highlighted the importance of DOC flocculation at the point where river water encounters higher salinity water for the settling and removal of Hg in Bothnian Bay estuaries, something that is currently not included in our model.

Figure 10 depicts the seasonality and figure 11 three vertical profiles in the Gotland Sea. It is seen how quickly Hg concentrations can change in this region and, depending on physical drivers, how different the seasonality of vertical mixing can be. At location A (Gotland Deep) Hg concentrations are around 1.5 pM for most of the year with a strong surface depletion (1 pM) during August and September. At location C, located at the opposite side of Gotland, the seasonality is reverse with the highest concentrations (1.2-1.4 pM) during August and September and much lower concentrations (0.9 – 1.1 pM) throughout the rest of the year.

In summary, our conclusion is similar to that of the North Sea, i.e. that better data on Hg inputs from rivers and a better resolution of the physical processes in the domain seem the most promising options for improving model performance. Especially in the Bothnian Bay, Hg cycling seems to be strongly influenced by terrestrial organic matter. In the central Baltic, we found that typically used kd values around log(k_d) = 5.5 are not sufficient to reproduce the observed Hg depletion in the surface waters. Here, as described in the methods section, we use a k_d based on Tesan et al. (2020) which is an order of magnitude higher and leads to improved correlation to observations (Table 4). In addition, a higher vertical resolution is advised as vertical transport has proven to be an issue with the current model setup. Due to the low model resolution below 150 m, numerical diffusion leads to an overestimation of mixing in the deep basins. Finally, for further model evaluation, it would be useful to increase the seasonal coverage of observations in the area.

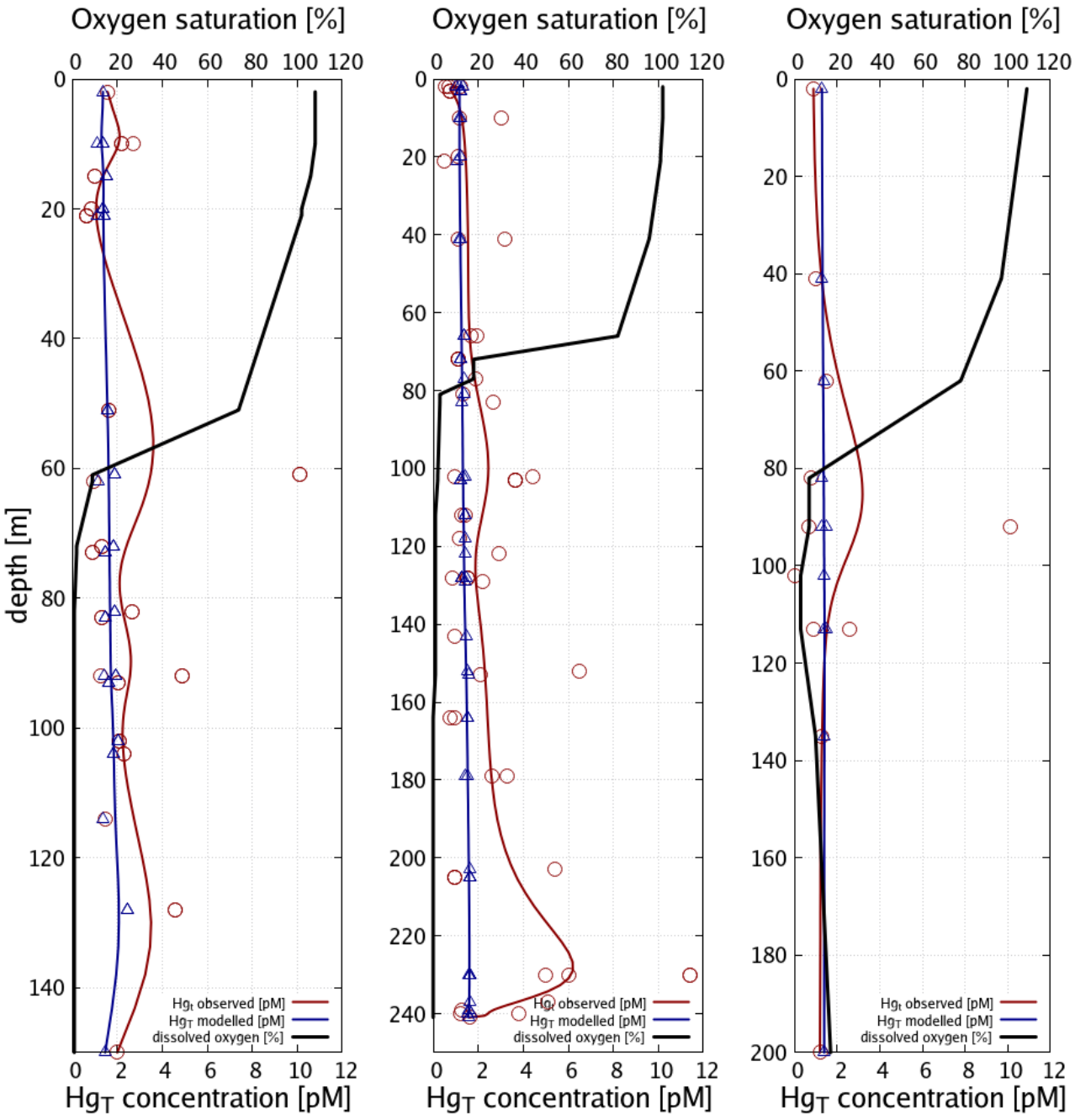

Figure 11: Vertical Hg profiles in the central Baltic Sea observations (blue) (Soerensen et al., 2018) and model values (red) for the three central Baltic deep basins given in Figure 9.

Finally, as the deep basins of the Baltic Sea are anoxic, in this area sulfur chemistry becomes relevant (R6-R9 Table 3). The effect of adding HgS and HgS-DOM to the chemistry scheme leads to particulate Hg-POM transforming into dissolved HgS species. The effect of this is two fold: (1) Firstly, Hg that is scavanged from the stratified surface layer by detritus (biological pump) accumulates directly at the boundary between oxic and anoxic waters.(2) Secondly, as eventually all inorganic Hg is transformed into HgS species, pareticle settling stops being a sink and Hg persists in the water column. Whereas Hg is effectively transported to the sediment in model runs without sulfur chemsitry. This leads to Hg concentrations being constant in the anoxic layer with higher values found only directly at the sea floor. Comparing to observations, we find that the model with sulfur chemistry is better able to capture the observed Hg distribution (Soerensen et al., 2018).

3.4.3 Elemental mercury (Hg0)

In the marine environment, elemental Hg^0 makes up only a few percent of the total Hg_T. However, it is the species that determines the air-sea exchange and thus is the major driver for atmospheric long-range transport. With the oceans being the largest Hg emitter into the atmosphere (roughly twice as large as current anthropogenic emissions), marine Hg^0 determines global transport patterns. Moreover, errors in modelled Hg^0 concentrations propagate to all other Hg species and lead to wrong estimates for the compartmental budgets. Thus, it is of utmost importance to correctly reproduce Hg^0 concentrations in surface waters. A detailed model study on Hg air-sea exchange in the North and Baltic Sea has been published using a previous model version (Kuss et al., 2014; Bieser and Schrum, 2015). The four main drivers of Hg^0 concentrations are:

1) The reducible fraction of Hg^{2+} which is typically estimated to be 40% of the dissolved $Hg^{2+}_{(aq)}$.
2) The parametrization of biologically induced reduction processes.
3) The modelled photon flux and wavelength-dependent extinction in water impacting photolytic reduction.
4) Air-sea exchange parametrizations, especially during high wind speeds.

Due to the fast exchange between atmosphere and water, Hg^0 concentrations converge towards the equilibrium as described by Henry's Law constant (Andersson et al., 2008). Therefore, in shelf seas a change in the red-ox chemistry directly affects the total Hg^T in the system. Due to the mixing in the coastal ocean, this impacts almost the complete water body. Moreover, the different reduction pathways produce a distinct seasonal pattern with Hg^0 concentrations ranging from as low as 5 pg/l during winter up to peaks > 60 pg/l during cyanobacteria blooms. Thus because of the high intra annual variability the model needs to be evaluated against Hg^0 observations throughout the year, as good agreement for a single cruise does not imply good model performance throughout the year.

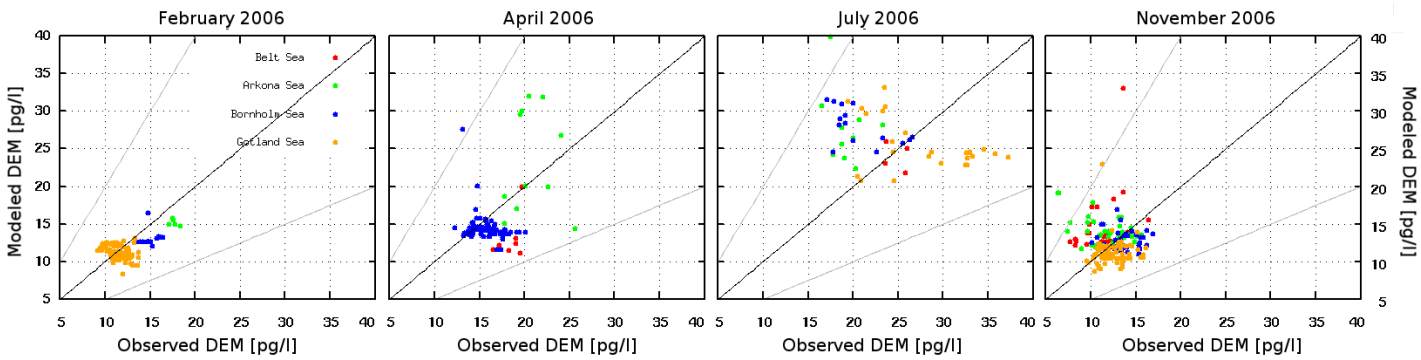

Figure 12: Comparison of modeled and observed Hg^0 concentrations in surface waters for four cruises in the Baltic Sea (x-axis: observations, y-axis: model values (Kuss et al., 2014).

obs mean	mod mean	NMB	NCRMSE	NMSD	FAC2	N
14.6	14.9	0.02	0.35	0.38	97%	477
obs std	**mod std**	**NMB_{crit}**	**RMSE**	**$NMSD_{crit}$**	**R**	**MQO**
4.60	6.30				0.60	0.84

Table 8: Comparison of modelled and observed Hg^0 concentrations for four Cruises in the Baltic Sea in 2006 (Kuss et al., 2014).

The observed annual average Hg^0 concentration for 580 measurements is 14.6 pg/l, the modelled value is 14.9 pg/l with a systematic error of 2% and a random error of 35%. The random error is largest in summer (NCRMSE=42%) and is due to the biogenic reduction which depends on cyanobacteria biomass. The model shows good correlation with observations (R=0.60) and is able to reproduce the observed variability (NMSD = 38%) (Table 8). All statistical metrics for Hg^0 are well inside model performance criteria and 97% of the model values are within a factor of 2 of the observations. The model quality objective is below 1.0 (MQO = 0.84). Thus, the model performance is, at least for the given model resolution, in the range where further improvements hardly feasible (Carnevale et al., 2014; Schutgens et al., 2016). We acknowledge, that the red-ox chemistry used is based on measurements in the Baltic Sea (Kuss et al., 2015). Thus, it needs to be investigated whether it shows equally good performance for other marine regions. We find, that the model performs similarly well throughout the year with the largest bias during summer where the dynamics driving biological and photolytic reduction lead to a higher variability of Hg^0 concentrations (Table 9).

	obs mean	mod mean	NMB	NCRMSE	NMSD	N
February	12.0	11.4	- 0.05	0.28	0.41	130
April	16.5	15.2	- 0.08	0.23	0.70	111
July	23.1	28.0	0.21	0.42	0.13	62
November	12.4	12.7	0.03	0.28	0.30	174

Table 9: Seasonal breakdown of Hg^0 model performance.

Figure 13 depicts the seasonality of a mean Hg^0 for the Baltic Sea. Moreover, the contribution of the four reduction reactions (1) chemical reduction, (2) photolytic reduction, (3) biogenic reduction, and (4) reductive methylation (Table 3) are given. We find, that the dark reduction is the dominant process, producing 55% of the total Hg0 in the Baltic Sea and 70% in the North Sea. Photolytic reduction contributes 34% and biogenic reduction contributes 12% annually. However, from July to middle August the photolytic reduction becomes dominant (>50%). When the cyanobacteria

bloom starts, light penetration reduces significantly due to the increased marine particle load and until the end of November the biogenic reduction becomes the dominant process (Figure 13a). In contrast, as there are no cyanobacteria in the North Sea, photolytic reduction is dominant throughout the summer (Figure 13b). The reductive methylation reaction plays a negligible role for Hg0 surface concentrations but can be a source for Hg0 in deeper waters with a high MeHg fraction. It can be seen, that there is a background Hg0 concentration of about 5 to 15 pg/l in due to the chemical (dark) reduction process. During model development, we recognized a systematic error in the seasonality (overestimation during summer and underestimation during winter) that could be resolved by introducing a temperature dependency of the chemical reduction reaction, a process which was detectable in the observations by Kuss et al. (2015) (Eq. 8, Section 2.3.1). For the photolytic reaction, we found that it is important to validate the radiation fields. Testing the model using different radiation fields resulted in a change of the annual net Hg0 production of > 10%. The main driver here is cloud coverage which is a particularly uncertain state variable in meteorological models. Moreover, we want to note that photolysis rates from observations and incubation experiments are solely reported based on the photolytically active radiation. Due to the highly wavelength selective light extinction it would be favourable to parameterize photolysis using the actual wavelengths absorbed by Hg. Finally, the biogenic reduction term in the model is driven only by the concentration of cyanobacteria. This creates the observed late summer / early autumn Hg0 peak. Allowing other phytoplankton species in the model to reduce Hg2+ lead to unrealistically high concentrations during the spring flagellate bloom.Figure 13: Annual profile of mean Hg0 concentration in the Baltic Sea (top) and North Sea (bottom). The colored areas indicate the contribution of individual reduction pathways (R1,R3,R20 Table 3).

Figure 13: Annual profile of mean Hg^0 concentration in the Baltic Sea (top) and North Sea (bottom). The colored areas indicate the contribution of individual reduction pathways (R1,R3,R20 Table 3).

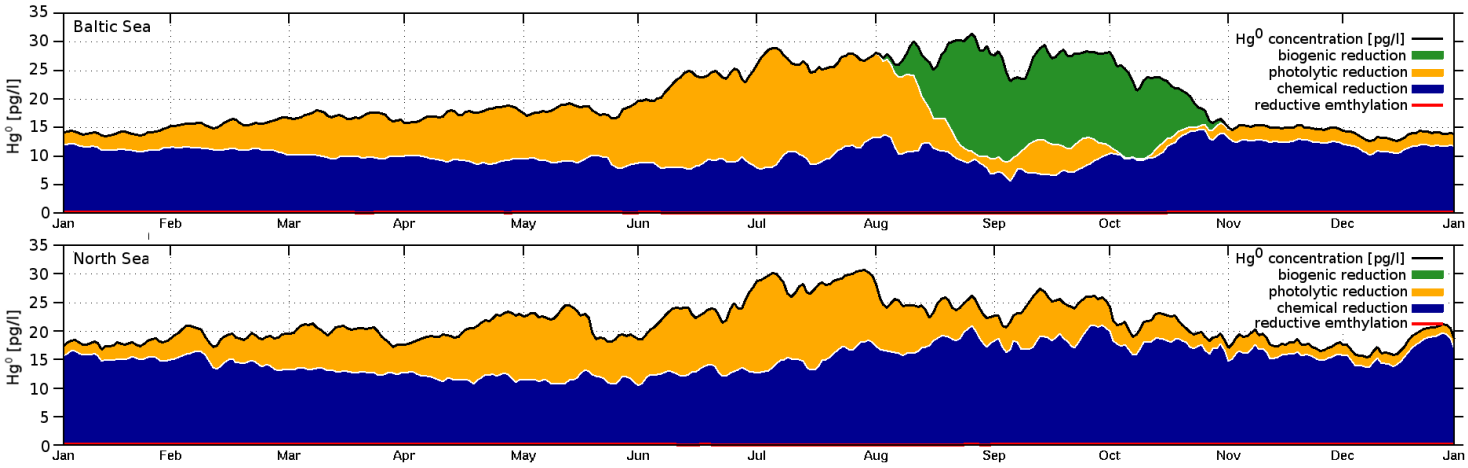

3.4.4 Methylmercury ($MMHg^+$ and DMHg)

Due to the complexity of the analytical methods and the extremely low environmental levels, MeHg observations in the marine environment are rare. Additionally, they are the most uncertain observations. Here, to calculate the MQO, we assume an uncertainty of 50%. We evaluate the model predictive capabilities in reproducing (1) MeHg concentrations and (2) the methylated Hg fraction M_{frac} = MeHg/Hg_T. The latter allows us to evaluate the modelled net methylation independent of the Hg_T model error (Table 10). In the Baltic Sea MeHg observed concentrations are in the range 191 fM (20 – 603) while the modelled range is 213 fM (57 – 350). For M_{frac} the observed range is 11.4% (1.3 – 30.4) (10^{th} and 90^{th} percentiles) while the model predicts 9.9% (3.6 – 20.2). The frequency distribution for observed and modelled M_{frac} is given in Figure 15. The model is in very good agreement with the observations on average but cannot reproduce the observed extreme values. In total there are 17 (6.5%) samples with a M_{frac} between 33% and 73%, all of which were measured in the intermediate layer between 70 and 160m.

Evaluating the relative M_{frac} metric instead of absolute MeHg concentrations reduces the systematic error from -28% to 5% and the amplitude error from -74% to -55%. This shows, that the Hg_T bias accounts for roughly 80% of the MeHg systematic error and 50% of the amplitude error. Yet, using M_{frac} has no significant effect on the random error indicating a non-linear relationship between the methylated fraction and the absolute amount of MeHg. While systematic error and amplitude error are comparable to the other Hg species, the random error is much larger (NCRMSE = 1.9). This shows that the methylation-demethylation dynamics in the model is too simplified, pointing to missing processes in the model. Figure 15 depicts MeHg and M_{frac} vertical profiles for the central Baltic Sea deep basins in different years and seasons together with oxygen concentrations. Again, it can be seen, that the model is able to reproduce the average vertical profiles but is incapable of capturing the high and low values. Observations indicate an MeHg hotspot near the oxycline. Here, M_{frac} can become as large as 100%, meaning that there almost all mercury is present as MeHg. The highest MeHg observations coincide with anoxic conditions indicating that the availability of dissolved HgS drives methylation in these regions (Soerensen et al., 2018). In Figure 15, anoxic regions are indicated by negative oxygen concentrations. These are based on measurements of H_2S and the net oxygen is calculated based on the reaction: $H_2S + 2O_2 \rightarrow H_2SO_4$.

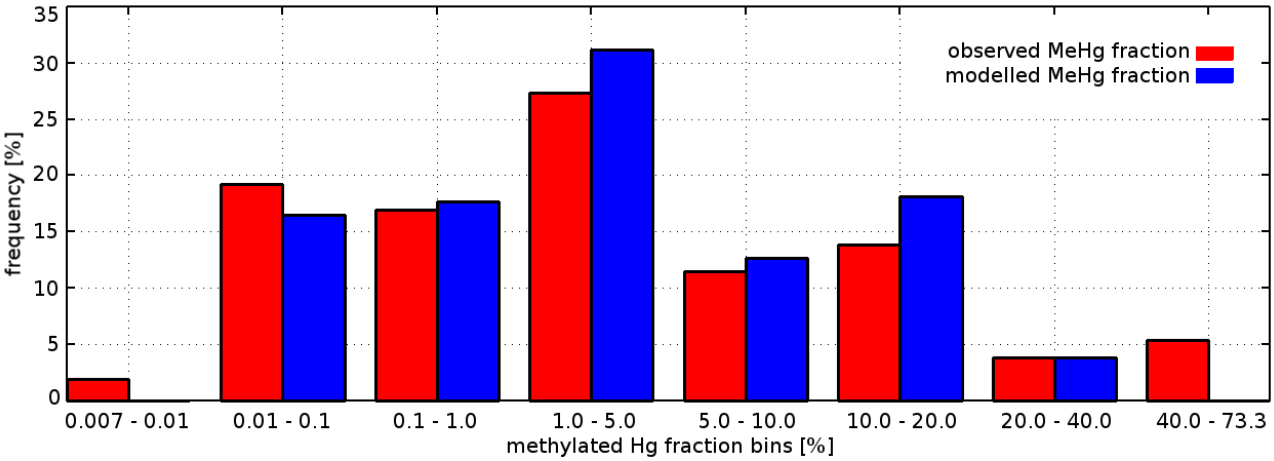

Figure 14: Observed (Kuss et al., 2017 and Soerensen et al. 2018) and modelled frequency distribution of the methylated Hg fraction M_{frac}..

Depth [m]	obs MeHg$^+$	mod MeHg$^+$	NMB	NCMRSE	NMSD	FAC2	MQO	obs M_{frac}	mod M_{frac}	N
Total	**191**	**213**	**0.11**	**1.9**	**- 0.55**	**53 %**	**0.98**	**11.4 %**	**9.9 %**	**160**
March										
0 – 250	**222**	**279**	**0.28**	**2.1**	**- 0.55**	**54 %**	**1.03**	**12.0 %**	**10.3 %**	**96**
0 – 50	73	88	0.22	1.3	- 0.54	60 %	1.00	6.3 %	5.2 %	40
50 – 150	230	257	0.12	1.7	- 0.67	47 %	0.95	15.0 %	12.2 %	45
150 – 250	734	1067	0.45	1.5	- 0.88	64 %	1.09	19.8 %	21.2 %	10
Jul – Sep										
0 – 250	**163**	**130**	**- 0.20**	**1.6**	**- 0.56**	**49 %**	**0.76**	**10.7 %**	**9.5 %**	**64**
0 – 50	53	42	- 0.20	1.6	- 0.67	59 %	0.83	6.3 %	5.0 %	29
50 – 250	263	144	- 0.45	1.4	- 0.70	46 %	0.73	17.8 %	12.9 %	28
150 – 250	248	174	0.11	4.2	- 0.68	17 %	3.21	3.80%	20.4 %	7

Table 10: Evaluation of seasonally and vertically clustered M_{frac} observations against model values.

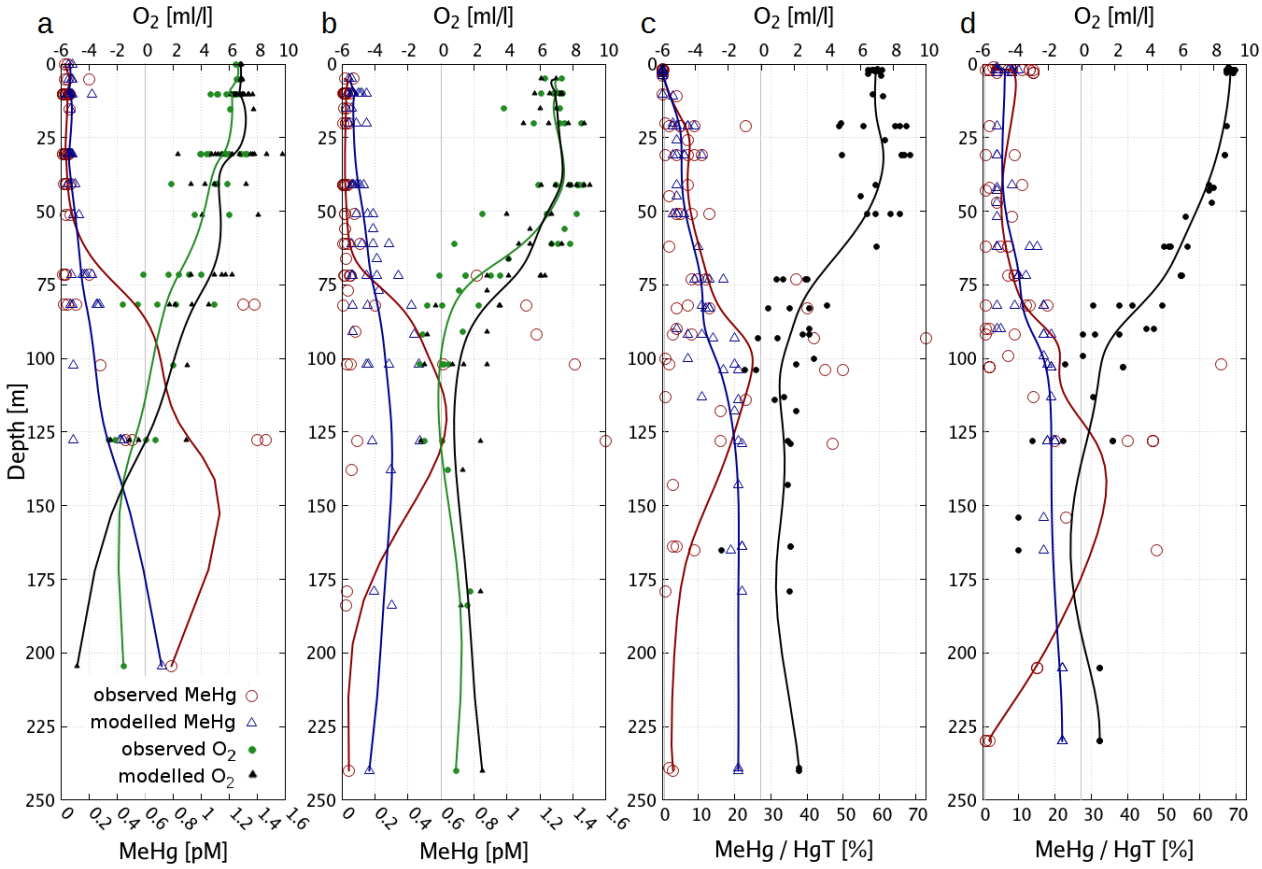

Figure 15: Vertical MeHg profiles for Baltic deep basins. Negative oxygen concentrations indicate sulfide concentrations. a) MeHg profiles 2014 (Soerensen et al., 2018), b) MeHg profiles 2015 (Soerensen et al., 2018), c) M_{frac} March (Kuss et al., 2017), d) M_{frac} July/August (Kuss et al., 2017).

The model can reproduce seasonality and vertical gradient of the methylated fraction. On the one hand photolytic demethylation leads to lower MeHg concentrations in the surface ocean during summer. On the other hand, biological activity leads to increased MeHg formation in spring and summer. We find, that a biologically induced methylation parameterized with biomass or phytoplankton concentration leads to spring becoming the season with the most effective net methylation. By linking biological methylation to the remineralization of organic carbon, we introduce a temperature dependency that shifts this towards summer (Figure 16) (Eq. 9, Section 2.3.1). Yet, the model still overestimates

methylation in spring and underestimates methylation in summer. For a more detailed analysis, we look at surface layer MeHg concentrations on four specific days. Figure 17 depicts MeHg measurements for 21st March and 1st August of the years 2014 and 2015. In March MeHg concentrations are between 40 and 300 fM and in August between 10 and 200 fM with pronounced spatial gradients. This 'spottiness' of the MeHg concentrations partially explains the large random error in the model. Moreover, while the general patterns are similar, methylation shows a significant inter annual variability (Figure 17).

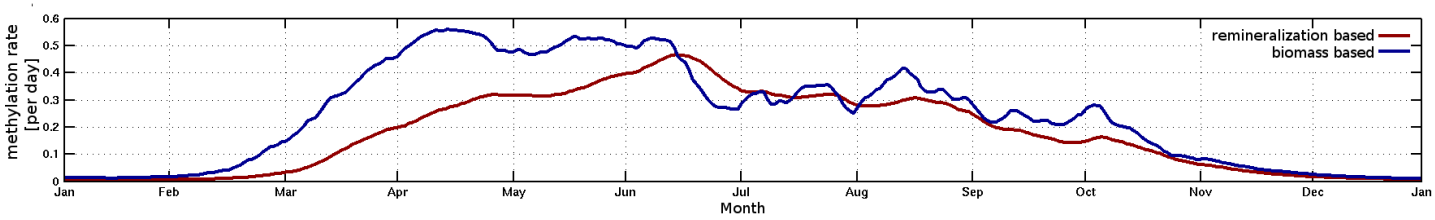

Figure 16: Seasonality of the biologically induced methylation reaction using different parametrizations (R12, Table 2).

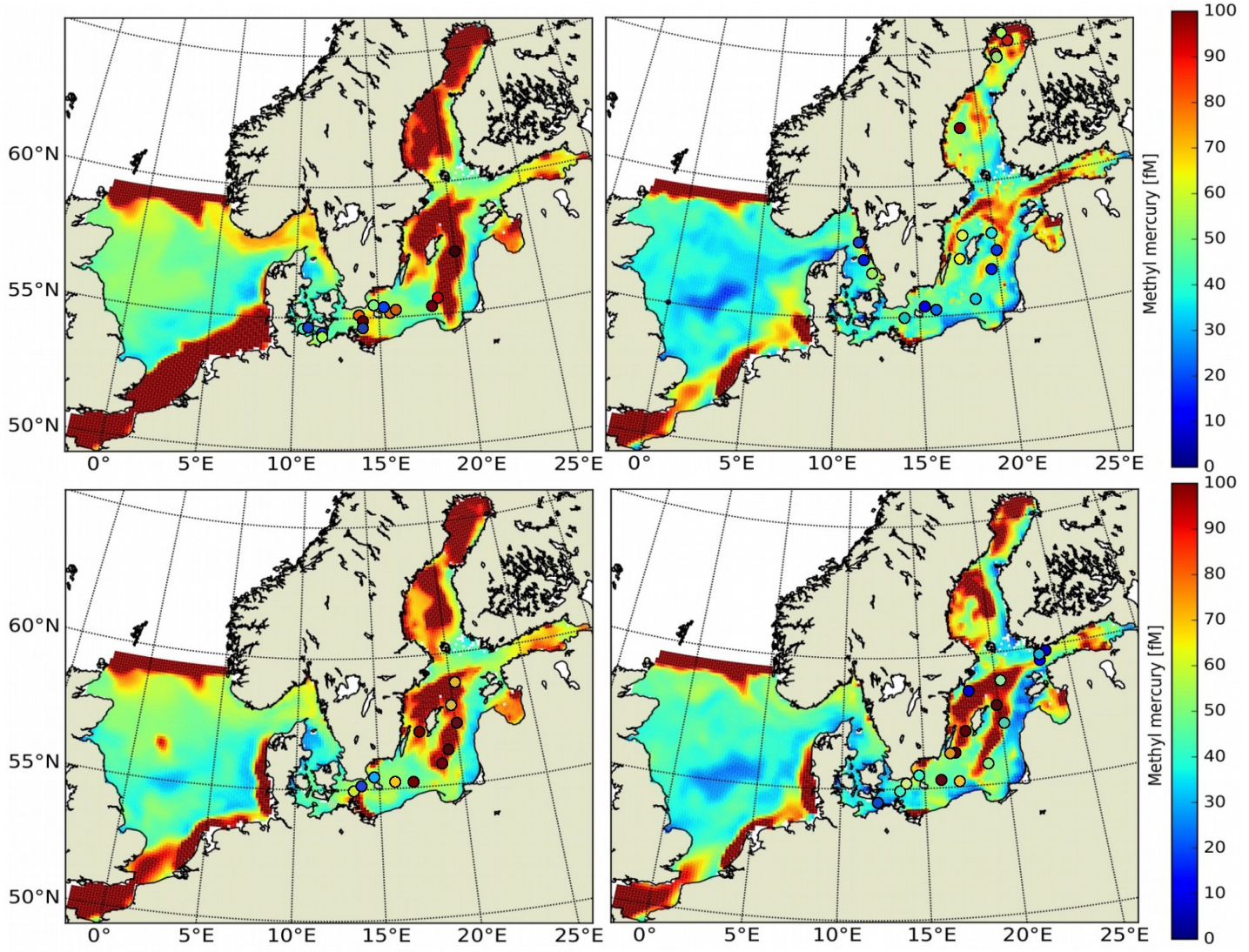

Figure 17: Methylmercury concentrations in the surface ocean on a) 21st Mar 2014 b) 1st Aug 2014 c) 21st Mar 2015 d) 1st Aug 2015 superimposed are all observations in depths of 0-50m (Table 9).

Overall, the model reproduces 53% of MeHg values within a factor of 2. We find that the model performance (MQO = 0.98) is still within the quality criterion. This is due to the much higher uncertainty of MeHg measurements for which we assumed an error of 50%. This indicates that further model improvement will be difficult unless more frequent and more precise MeHg measurements become available. Moreover, to reach their full potential MeHg observations need to be combined with extensive auxilliary data. This starts with simple parameters like incoming solar radiation to determine the actual intensity of photolysis or better estimates for special partitioning coefficients for MeHg. In our model, for example, we use a lower k_d of $MMHg^+$ compared to Hg^{2+} which means that particle settling will increase M_{frac} with increasing depth (Table 4, Section 3.2.3). Moreover, chemical parameters such as O_2 and H_2S concentrations have been shown to impact the availability of inorganic Hg^{2+} species for methylation. And finally, microbiological observations ranging from chlorophyll concentration to RNA showing the activity of methylating bacteria could improve variable methylation rates. From our model evaluation it seems clear that fixed methylation and demethylation rates cannot account for the observed variability in both MeHg concentrations and fraction M_{frac}. Here, we need a better understanding of the parameters modulating methylation and demethylation rates.

3.4.5 Hg in biota

Figure 18 depicts annual average Hg loads in the different ecosystem biota species. The North Sea exhibits higher Hg loads in biota which can be explained by the high Hg load from rivers, especially Elbe and Schelde, the lack of permanent sedimentation and the earlier onset and higher overall primary production which increases the effectiveness of the active uptake pathway. The average amount of Hg in biota ranges from 1% to 5% of the Hg_T with higher values in the highly productive North Sea. During winter only a little Hg is bound in biota due to the low biomass while in summer the fraction can be up to 10%. Due to the high transfer efficiency of $MMHg^+$ (97%), on average, between 5% and 20% of the total $MMHg^+$ is accumulated in biota. In highly productive regions the amount of $MMHg^+$ inside biota can even be larger than the $MMHg^+$ remaining in the water column. Flagellates (Figure 18b) are the most abundant phytoplankton species and thus the most important primary accumulator. However, the diatom bloom occurs earlier in the year and removes MeHg from the water column before the flagellate bloom. The higher Hg load in diatoms (Fig 18a) is due to their lower carbon content. Finally, cyanobacteria (Figure 18c) which can lead to major blooms in late summer / early autumn are the dominant species later in the year and MeHg loads during the bloom exceeds those of the diatoms and flagellates. Due to the active Hg uptake, micro (Figure 18d) and meso zooplankton (Figure 18e) have a higher accumulation factor than the phytoplankton species. Finally, figure 18f depicts the Hg load in fish.

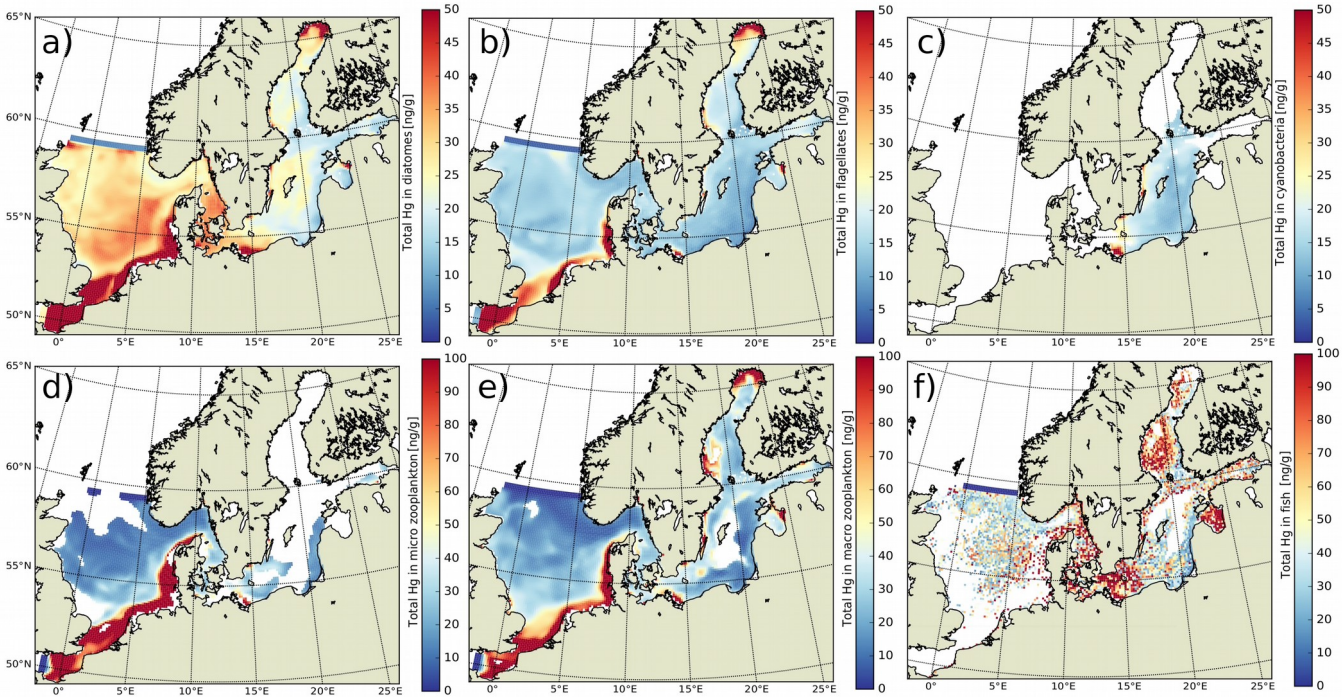

Figure 18: annual average Hg_T concentrations [ng/l] in biota: a) diatoms, b) flagellates, c) cyanobacteria, d) micro zooplankton, e) meso zooplankton, f) fraction of Hg in fish.

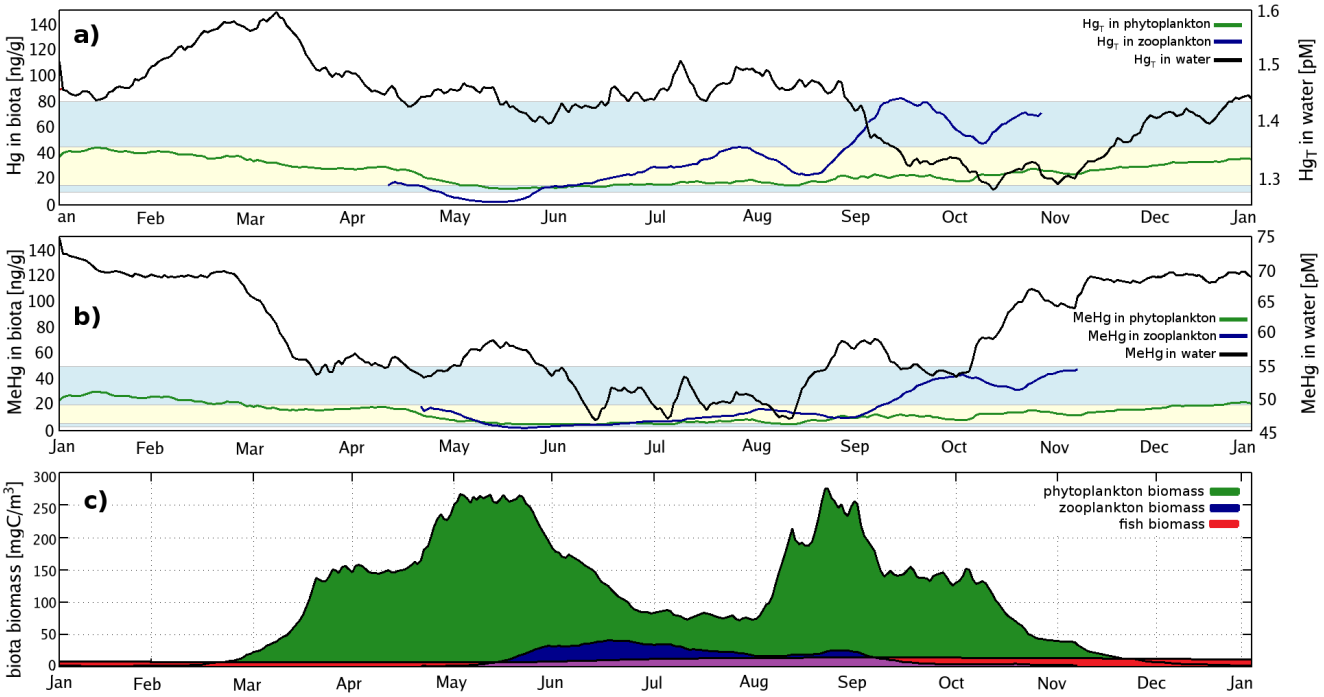

Figure 19: Seasonality of modelled a) Hg and b) MeHg loads in phytoplankton and zooplankton. Superimposed is the water concentration of a) Hg and b)= MeHg. c) gives the integrated biomass. All values are averages for the Baltic Sea integrated over the top 100m.

As the last step of the model evaluation, we compare HgT and MeHg loads in biota to observations. Field studies investigating the total Hg content of biota are fairly common and can be used to estimate the model bias. However, only little data on MeHg in biota and species diversity is available. On average the observed HgT content in phytoplankton lies in the range of 0.002±0.001 µg/g wet weight and that for zooplankton in the range of 0.006±0.005 µg/g wet weight (Nfon et al. 2009). Here, we use a conversion factor for wet weight (w.w.) to dry weight (d.w.) of 0.2 for phytoplankton and 0.16 for zooplankton (Cushing 1958; Ricciardi and Bourget 1998). Moreover, biomass in ECOSMO is defined in mgC, whereas observations are reported in mg wet weight (ww) or mg dry weight (dw). We estimate the ratio of mgC to mg dw as: 0.2 for diatoms, 0.33 for flagellates and cyanobacteria, and 0.5 for zooplankton (Sicko-Goad et al. 1984; Walve and Larsson 1999). With this, we estimate the expected average HgT loads in biota in the Baltic Sea in the range of 30 (15–45) ng/gC in phytoplankton and 75 (10–120) ng/gC in zooplankton. MeHg loads in phytoplankton are expected to be around 10 (5-15) ng/g d.w. while being larger for cells with a larger surface to volume ratio (Pickhardt and Fisher 2007; Soerensen et al. 2016). Figure 19 depicts the average HgT and MeHg loads in phytoplankton and zooplankton. For phytoplankton, the model lies well within the expected range for HgT (25-80 ng/gC) (Figure 19a) and MeHg (5-15 ng/gC) (Figure 19b). During winter when phytoplankton biomass is low (Figure 19c), Hg loads reach the maximum of the expected bioaccumulation range and once production starts growth dilution lowers the modelled HgT and MeHg loads and their concentrations in the water column declines by 10% and 20% respectively. For zooplankton, values are well within the expected range. They start low in the beginning and rise over the year. At the end of the year, cyanobacteria start to dominate the phytoplankton community leading to higher phytoplankton MeHg concentrations and another decline in marine HgT concentrations. At the same time, the decrease in diatom and flagellate concentration lead to an increase in the fraction of microzooplankton of the mesozooplankton diet, increasing their trophic level and further increasing the zooplankton HgT load. Finally, with Hg loads between 70 and 140 ng/gC dw, fish are the highest trophic level in the ecosystem model. Due to the much more efficient active uptake of $MMHg^+$ compared to Hg^{2+} in fish 60 to 80% of the accumulated Hg is in the form of $MMHg^+$. Looking at the two uptake pathways of bioconcentration and biomagnification we find that biomagnification is responsible for 80 to 90% of the total Hg uptake for non-phytoplankton species. A more detailed analysis can be found in Amptmeijer et al. (2023).

Next, we evaluate the model capabilities to reproduce Hg content in fish. For this, we compare the modelled bioaccumulation in the functional ecosystem group representing fish to herring. This pelagic species corresponds best to the fish functional group implemented into ECOSMOS (Daewel and Schrum, 2019). The analysis is based on 1166 measurements of Hg in fish muscle tissue. We use the same conversion factors as for zooplankton to convert the model carbon dry weight to wet weight total biomass (1 ng/gC d.w. = 3.125 ng/g ww). For this, the dataset is split into five Baltic Sea regions:

(1) The Swedish West Coast, a stripe from Goteborg to Oslo

(2) The Southern Baltic Proper which includes the Bornholm Sea and the southern Gotland Sea

(3) The Northern Baltic Proper which includes most of the Gotland Sea

(4) The Bothnian Sea

(5) The Bothnian Bay

It is not possible to compare the catched fish to an individual model grid cell and timestep. Therefore, we compare to observed average Hg_{Fish} concentrations. The model reproduces the observed average Hg_{Fish} of 28 ng/g in the Baltic Sea with a systematic error of -9% (Hg_{Fish} = 25 ng/g) (Table 11). In order to estimate the model variability of Hg_{Fish} for each region we vertically integrate annual average model values for each grid column. The result is a fish dataset in which each member represents a model fish that has spent its life in a single 10x10 km² water column. In reality, herring are not confined to 10x10 km² grid cells and their Hg accumulation depends on their migration patterns. Yet, we argue that this approach approximates the model spread (Figure 20). This allows us to calculate not only the bias but also to estimate the model standard deviation. On average, over the whole Baltic Sea, the model captures the observed variability (NMSD = 9%). The error is driven by the West Coast region (NMSD = 309%) while it varies between (29% – 76%) in the remaining Baltic Sea. In the West Coast region, the observed fish exhibit less than half the variability observed in all other regions. While the model captures the variability in the other regions it shows the opposite behavior as the observations in the West Coast. In this shallow region, we explain the high model concentrations with regular Hg resuspension from sediments which create pockets of elevated Hg_T and MeHg concentrations. Thus, the large model spread is an artefact of our methodology based on static fish.

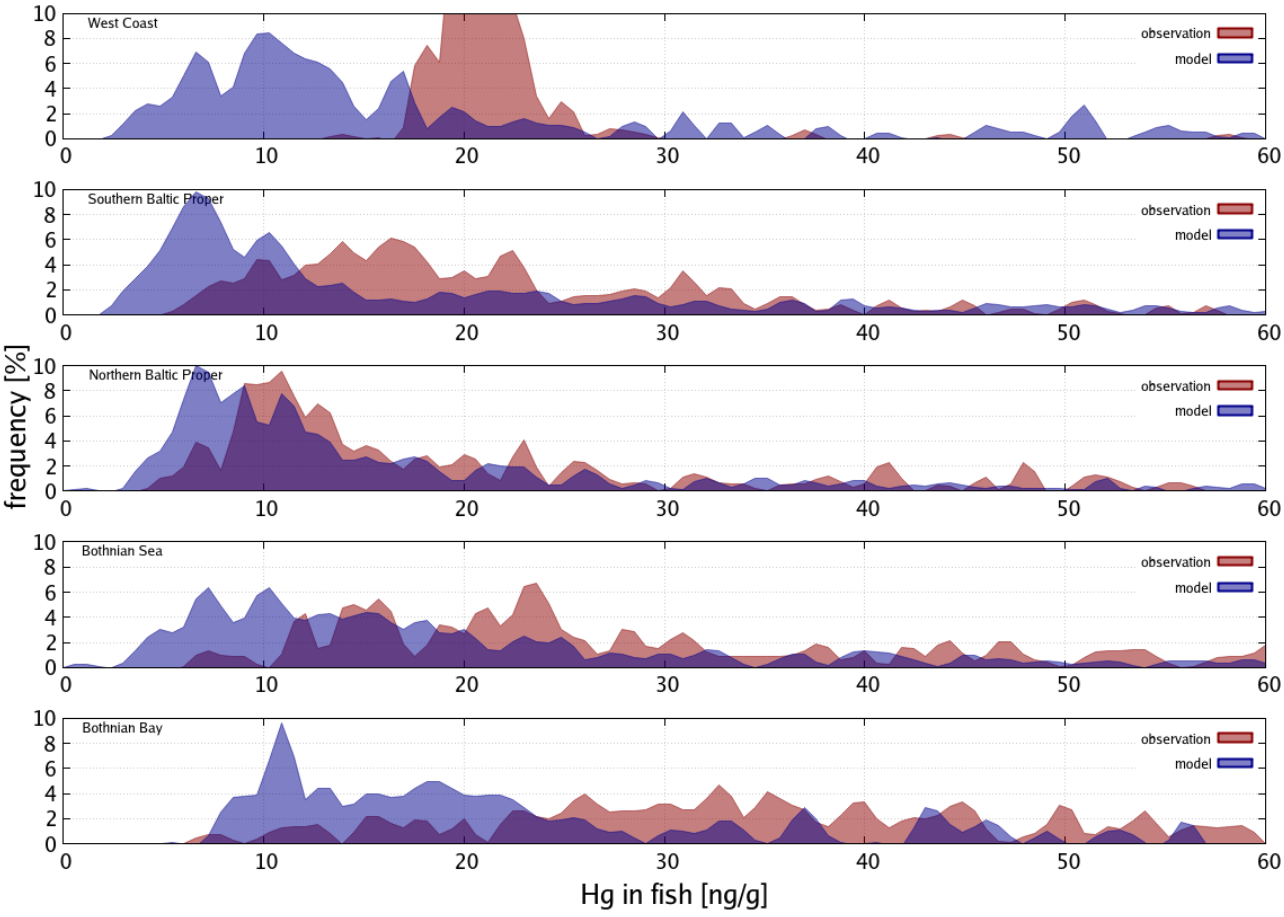

Figure 20: Modelled and observed frequency distribution of Hg in fish in Baltic Sea regions (Soerensen and Faxneld 2020).

4 Conclusions

In this paper, we present the regional scale 3D high-resolution biogeochemical multi-media Hg model MERCY v2.0. The numerical model combines hydrodynamic models for atmosphere and ocean including a marine ecosystem model. MERCY includes a comprehensive marine Hg scheme to calculate transport, transformation and bio-accumulation. The schemes for chemistry, partitioning, and bioaccumulation are based on literature values and no domain-specific model tuning has been done. We would like to emphesize that MERCY is applicable for any marine region or even for global application. The major factors when applying the MERCY model to other regions are (1) partitioning coefficients to organic material (OM) as the type of OM varies regionally, (2) the parametrization for biogenic reduction as the values presented here are based on cyanobacteria in the Baltic Sea, and (3) the ecosystem model, as trophic dynamics and phytoplankton uptake rates can vary widely between regions. To our knowledge, it is the first model capable of linking atmospheric Hg emissions to MeHg accumulation in higher trophic levels. The intention of this initial model publication is the detailed presentation of the model and first results focusing on model performance evaluation and the identification of the processes and parameters responsible for the model error. A more comprehensive analysis of the dynamics and variability of Hg speciation, partitioning, and bioaccumulation is required for future studies. While our model performs more realistically than earlier models for marine Hg cycling, there are still large uncertainties, especially regarding methylation.

	mean (10^{th} – 90^{th} percentile)		**model error**			**performance criteria**		
Hg species	**observation**	**model**	**systematic**	**random**	**amplitude**	**FAC2**	**MQO**	**N**
Hg_T	2.69 pM (0.9 – 6.0)	2.24 pM (1.1 – 3.7)	- 17 %	67 %	- 55 %	72 %	1.44	435
Hg^0	73.2 fM (53 – 99)	74.6 fM (52 – 123)	2 %	35 %	38 %	97 %	0.84	477
MeHg	190 fM (20 – 612)	135 fM (48 – 270)	- 28 %	160 %	- 74 %	49 %	0.80	264
MeHg / Hg_T	11.4 % (1.3 – 30)	9.9 % (3.6 – 20)	- 5 %	190 %	- 55 %	53 %	0.98	160
Hg in fish	28 ng/g (12 – 52)	25 ng/g (6 – 71)	3 %	n/a	9 %	n/a	n/a	1166

Table 12: Model performance evaluation of Hg_T, dissolved elemental Hg^0, and the methylated Hg fraction. The model error is separated into systematic error (normalized bias), random error (normalized centred root mean square error), and amplitude error (normalized mean standard deviation). The model quality objective target value is MQO < 1.0 (consult Section 3.1 for more information).

We evaluated model performance for key Hg species based on a simulation for the North and Baltic Sea for the years 2000 to 2016. We chose these regions due to the availability of observations. Moreover, the two regions covers a range of regimes, has high primary productivity and is relevant for fisheries. Unlike atmospheric Hg modelling, there is no precedent or scientific consensus defining the state-of-the-art requirements and limitations of reproducing concentrations of different marine Hg species. Considering the inherent uncertainty of a comparison of model values and observed concentrations (e.g. measurement error, sampling error, error of the hydrodynamic models, the uncertainty of reaction rates, and unknown processes) we define model values within a factor of 2 of the observations as a reasonable agreement. Moreover, we used a statistical model quality objective (MQO < 1.0) to assess the model skill (Carnevale et al., 2014) (Section 3.1).

A detailed model performance evaluation for the North and Baltic Sea demonstrates that the model can reproduce concentrations and seasonality of single Hg species to a degree that validates the model predictive capabilities. For Hg_T, the model is able to reproduce 72% of the observations within a factor of 2 (Table 12). We find that the model can repro-

duce background concentrations in the open parts of the shelf seas (1.0 – 1.5 pM). The model error can mostly be attributed to random and amplitude error. The main source of uncertainty in the model is the transport dynamics of the large Hg influx from rivers and the Wadden Sea. These lead to observed Hg peaks of up to 10pM. The model resolution of 10x10km proved insufficient to reproduce the observed temporal and spatial gradients. Because the majority of observations are at the coast near major rivers, the model does not reach the quality objective (MQO = 1.44). Moreover, in the Baltic Sea, the model overestimates vertical mixing from deeper regions with elevated Hg concentrations. This is caused by the coarse vertical resolution below 150 m which leads to numerical diffusion and an underestimation of stratification. We found that including sulfur chemistry improves model performance in the deep anoxic water layer in the Batlic Sea basins. The mechanism is, that Hg transported downwards from the stratified oxic und productive surface layer through the biological pump transforms into dissolved HgS species in anoxic waters. This stops the downward gradient and lessens the role of the sediments in this region as a sink.

We summarize the improvement of the model performance for Hg_T requires optimizing of the hydrodynamic model. Unless circulation patterns, stratification seasonality, resuspension events and upwelling regions are correctly represented hardly any improvement of the model can be achieved. Further, for the coastal ocean, we find that river inflow needs to be better resolved, ideally with daily loads including fluxes of dissolved and particulate carbon. Finally, particle partitioning and subsequent sedimentation is a major source of uncertainty. We achieved better results using a $\log(k_d)$ of 6.6 (Tesan et al., 2020) which is an order of magnitude higher than those used by other models.

The model performed best for elemental Hg^0. Due to air-sea exchange, Hg^0 is the key species controlling the exchange between atmosphere and ocean. Any bias in modelled Hg^0 fields directly influences the marine total Hg budget and leads to unrealistic results. MERCY is able to reproduce 97% of Hg^0 measurements within a factor of 2. We find that the chemical (often referred to as dark) and photolytic reduction processes produce roughly the same amount of Hg^0 annually although with different seasonality. Moreover, elevated Hg^0 concentrations in the Baltic Sea between July and October could be reproduced by implementing biological reduction by cyanobacteria. Finally, we find that it is important to consider temperature dependence for the chemical reduction reaction to correctly reproduce the seasonality. With a model skill of MQO = 0.84 we conclude that the model performance for Hg^0 is in a range where further improvements become marginal. Possible improvements are photolytic reaction rates based on actual wavelengths instead of the photolytic active radiation, and a better understanding of biological reducers.

Evaluation of MeHg resulted in the methylated fraction M_{frac} ($MeHg/Hg_T$) for which 55% of model values are within a factor of 2 of observations. The model is able to reproduce the observed mean and seasonality but is unable to capture the observed maxima resulting in a large random error. Yet, because of the high measurement uncertainty the model still reaches the quality objective (MQO = 0.98) indicating that the observations are limiting model development. We found that in order to produce realistic MeHg concentrations throughout the year required methylation occurring in oxic waters. Oxic methylation is the primary or sole source (80% – 100%) of MeHg in large parts of the model domain. The anoxic methylation reaction is dominant in anoxic waters (the deep basins of the Baltic Sea). We found that assumptions made in other models linking methylation to productivity or chlorophyll concentrations pose two problems:Firstly, they lead to regions with zero MeHg in seasons with no primary production and very low MeHg concentrations in the deep anoxic basins. And secondly, they produce a phase error in the seasonality due to an overestimation of MeHg during the spring bloom. In MERCY, we parameterize the biogenic methylation with the amount of remineralized organic matter, which adds a temperature dependence to the process which in turn reduces the impact of the spring bloom. Moreover,

various sensitivity runs using varying parameters to modulate the biogenic methylation rate to test for possible biological drivers have failed to surpass model formulations including a constant oxic methylation reaction. We summarize that poor model performance for MeHg is the key source of uncertainty in the presented model. In order to improve the model performance a more detailed understanding of methylation processes is required. Moreover, more high-quality observations, especially on MeHg seasonality are needed to allow for model-based process studies. The addition of isotopic fractionation to the model might also help to further constrainment of sources and sinks of MeHg.

Finally, we evaluate the model's ability to reproduce Hg in biota. Our model provides Hg and MeHg loads in phytoplankton, zooplankton, and fish which are inside of the observed range. We find that the modelled phytoplankton concentrations are varying within the observed maximum and minimum loads. Zooplankton changes in trophic level over the course of the year due to changes in diet. As expected, the model predicts the highest MeHg loads in fish making up 90% of the total Hg in fish due to its high transfer efficiency. Most parameters used for bioaccumulation are highly uncertain and there is ample room for improvement in this part of the model. We hypothesize that the ecosystem model which is focused on correctly reproducing carbon fluxes needs improvements regarding functional traits relevant for bioaccumulation such as size, shape, or feeding behaviour.

The presented model allows hypothesis testing within a consistent physical-biological-biogeochemical framework based on basic principles. We are currently working on a model version that allows for seamless coupling with different hydrodynamic ocean and marine ecosystem models to increase the applicability of the model. The model performance is here only cursory evaluated to limit the length of the paper For the future, we plan to investigate the sources of model uncertainty and sensitivity in order to identify the unsufficient understanding of the processes and find out the imprecise or unknown parameters, especially concerning methylation and biological uptake. Finally, we want to employ and promote the MERCY model as a tool for hypothesis testing and prediction within a consistent physical-biological-biogeochemical framework based on basic principles. This will enable researchers to (1) improve our understanding of the natural variability from seasonal to decadal time scales, (2) investigate forcing dynamics, leading to MeHg accumulation in seafood and (3) to estimate the impact of anthropogenic and natural drivers in support of the Minamata Convention on mercury.

Author contributions

Contributor role	Role definition *following CrediT taxonomy: https://credit.niso.org/*	Authors
Conceptualization	Ideas; formulation or evolution of overarching research goals and aims.	
	… for the mercuy model	JB
	… for the bioaccumulation model	DA, UD, JB
Methodology	Development or design of methodology; creation of models	
	… Hg chemical mechanism	JB, JK, ALS
	… Hg and MeHg bioaccumulation	DA, JB
Software	Programming, software development; designing computer programs; implementation of the computer code and supporting algorithms; testing of existing code components.	
	… for HAMSOM and ECOSMO	UD
	… for MERCY	JB
Validation	Verification, whether as a part of the activity or separate, of the overall replication/reproducibility of results/experiments and other research outputs.	JB
Formal analysis	Application of statistical, mathematical, computational, or other formal techniques to analyze or synthesize study data.	
	… for Hg_T and MeHg concentrations	JB
	… for Hg^0 concentrations and air-sea exchange	JB, JK
	… for Hg and MeHg bioaccumulation in lower and higher trophic levels	DA, ALS
Investigation	Conducting a research and investigation process, specifically performing the experiments, or data/evidence collection.	JB, JK, ALS
Resources	Provision of study materials, reagents, materials, patients, laboratory samples, animals, instrumentation, computing resources, or other analysis tools.	CS
	… Hg and MeHg observational data	JK, ALS
Data Curation	Management activities to annotate (produce metadata), scrub data and maintain research data (including software code, where it is necessary for interpreting the data itself) for initial use and later reuse.	ALS, JK, UD
Writing – original draft preparation	Creation and/or presentation of the published work, specifically writing the initial draft (including substantive translation).	JB, ALS, DA
Writing – review and editing	Preparation, creation and/or presentation of the published work by those from the original research group, specifically critical review, commentary or revision – including pre- or post-publication stages.	ALS, CS, DA, JK, FS
Visualization	Preparation, creation and/or presentation of the published work, specifically visualization/data presentation.	JB
Supervision	Oversight and leadership responsibility for the research activity planning and execution, including mentorship external to the core team.	JB, CS
Project administration	Management and coordination responsibility for the research activity planning and execution.	JB, CS
Funding acquisition	Acquisition of the financial support for the project leading to this publication.	CS, JB

Code availability

Source code: The MERCY v2.0 source code is freely available at https://zenodo.org/record/7101217

DOI: 10.5281/zenodo.7101217

License: CC-4.0 license

Contact: johannes.bieser@hereon.de

Driving models:

COSMO-CLM v4.0 is freely available at:
https://doi.org/10.5281/zenodo.5939757

CMAQ v4.7.1 is an active open-source development project of the U.S. EPA that consists of a suite of programs for conducting air quality model simulations. The model is freely available at :
https://doi.org/10.5281/zenodo.1079879.

HAMSOM-ECOMSO_2e2 v1.0 is freely available at:
https://doi.org/10.5281/zenodo.7587005
The code is also available from the Helmholtz Centre Geesthacht git repository:
https://coastgit.hzg.de/udaewel/hamsom-ecosmoe2e/

Competing interests.

The authors declare that they have no conflict of interest.

Acknowledgements

We want to thank all data providers for their invaluable input without which we would not have been able to develop the MERCY model. Special thanks to Lars-Eric Heimbürger-Boavida for the fruitful discussions on marine Hg cycling and Franz Slemr for sharing his vast knowledge on atmospheric chemistry and Hg cycling and fpr proof reading the final paper.

This work was funded by the H2020 project iGOSP under the ERA-PLANET program (Grant agreement no: 689443), the Marue Sklodowska-Curie Innovative Training Network GMOS-TRAIN (Grant agreement no: 860497) and the Program Oriented Funding POV-4 of the. Helmholtz Association of German Research Centres. ALS acknowledge financial support from the Swedish Research Council Formas (grant no: 2021-00942).

References

Andersson, M. E., Sommar, J., Gårdfeldt, K., and Lindqvist, O: Enhanced concentrations of dissolved gaseous mercury in the surface waters of the Arctic Ocean, *.Mar. Chem*., 110(3−4), 190−194, 2008.

Amos, H. M., Jacob, D. J., Holmes, C. D., Fisher, J. A., Wang, Q., Yantosca, R. M., Corbitt, E. S., Galarneau, E., Rutter, A. P., Gustin, M. S., Steffen, A., Schauer, J. J., Graydon, J. A., Louis, V. L. St., Talbot, R. W., Edgerton, E. S., Zhang, Y., and Sunderland, E. M.: Gas-particle partitioning of atmospheric Hg(II) and its effect on global mercury deposition, Atmos. Chem. Phys., 12,591–603, https://doi.org/10.5194/acp-12-591-2012, 2012

Amptmeijer, D.J., Mikheeva, E., Daewel, U., Bieser, J., Schrum, C.: The impact of ecosystem interactions on marine mercury and methylmercury concentrations in the North-and Baltic Seas. (in prep.).

AMAP / UNEP, 2019: Technical Background Report for the Global Mercury Assessment 2018. Arctic Monitoring and Assessment Programme, Oslo, Norway/UN Environment Programme, Chemicals and Health Branch, Geneva, Switzerland. viii + 426 pp including E-Annexes.

Amos, H.M., Jacob, D.J., Streets, D.G., Sunderland, E.M.: Legacy impacts of all-time anthropogenic emissions in the global mercury cycle, Global Biogeochem. Cycles , 27, 410-421, 2013.

Bieser J., Matthias, V., Travnikov, O., Hedgecock, I.M., Gencarelli, C., De Simone, F., Weigelt, A., Zhu, J.: Diagnostic evaluation of bromine reactions on mercury chemistry. In Steyn, D., Chaumerliac, N., Air pollution modeling and its application XXIV, Springer Proceedings in Complexity, pp. 519-523, 2016.

Bieser, J. and Schrum, C.: Impact of marine mercury cycling on coastal atmospheric mercury concentrations in the North and Baltic Sea region. Elementa 000111, 2016.

Bowman, K.L., Lamborg, C.H., and Agather, A.M.: A global perspective on mercury cycling in the ocean. Sci. Total Environ., 710, 25, 136-166, 2020.

Capo E, Bravo AG, Soerensen AL,Bertilsson S, Pinhassi J, Feng C,Andersson AF, Buck M and Björn E. (2020) Deltaproteobacteriaand Spirochaetes-Like Bacteria AreAbundant Putative MercuryMethylators in Oxygen-DeficientWater and Marine Particlesin the Baltic Sea.Front. Microbiol. 11:574080.doi: 10.3389/fmicb.2020.574080

Carnevale, C., Finzi, G., Pederzoli, A. et al. (2014) Applying the delta tool to support the Air Quality Directive: evaluation of the TCAM chemical transport model. Air Qual Atmos Health **7,** 335–346. https://doi.org/10.1007/s11869-014-0240-4

Christensen, J. H., Brandt, J., Frohn, L.M., and Skov, H. Modelling of mercury in the Arctic with the Danish Eulerian Hemispheric Model, Atmos. Chem. Phys., 4, 2251-2257, 2004.

Cohen, M., Draxler, R.R., Artz, R.S., Blanchard, P., Gustin, M.S., Han, Y.-J., Holden, T.M., Jaffe, D.A., Kelley, P., Lei, H., Loughner, C.P., Luke, W.T., Lyman, S.N., Niemi, D., Pacyna, J.M., Pilote, M., Poissant, L., Ratte, D., Ren, X., Steenhuisen, F., Steffen, A., Tordon, R., and Wilson, S.J.: Modeling the global atmospheric transport and deposition of mercury to the Great Lakes; Elementa, 4,000118, 2016.

Cossa, D., Heimbürger, L.-E., Pérez, F.F., García-Ibáñez, M.I., Sonke, J.E., Planquette, H., Lherminier, P., Boutorh, J., Cheize, M., Lukas, J., Barraqueta, M., Shelley, R., and Sarthou, G.: Mercury distribution and transport in the North Atlantic Ocean along the GEOTRACES-GA01 transect, Biogeosci., 15, 2309–2323, 2018.

Cressie, N.: The origins of kriging, Mathematical Geology, 22(3), 239-252, doi:10.1007/BF00889887, 1990.

Cushing, D H.: The estimation of carbon in phytoplankton. In:Rappt. Proces-Verbaux Reunions,Conseil Perm. Intern. Exploration Mer, 144, pp. 32–33, 1958.

Dastoor, A., Ryzhkov, A., Durnford, D., Lehnherr, I., Steffen, A., and Morrison, H.: Atmospheric mercury in the Canadian Arctic.Part II: Insight from modeling, Sci. Total Environ., 509–510, 16–27, https://doi.org/10.1016/j.scitotenv.2014.10.112, 2015.

De Simone, F., Gencarelli, C. N., Hedgecock, I. M., and Pirrone, N.: Global atmospheric cycle of mercury: a model study on the impact of oxidation mechanisms, Environ. Sci. Pollut. R., 21, 4110–4123, 2014.

Derwent D, Fraser A, Abbott J, Willis P, Murrells T (2010) Evaluating the performance of air quality models (No. Issue 3). Department for Environment and Rural Affairs.

Durnford, D., Dastoor, A., Ryzhkov, A., Poissant, L., Pilote, M.,and Figueras-Nieto, D.: How relevant is the deposition of mer-cury onto snowpacks? – Part 2: A modeling study, Atmos. Chem. Phys., 12, 9251–9274, https://doi.org/10.5194/acp-12-9251-2012, 2012

Fischer, H., and Matthäus, W.: The importance of the Drogden Sill in the Sound for major Baltic inflows. J. Mar. Sys. 9, 137-157, 1996.

Green NW, Heldal HE, Måge A, Aas W, Gafvert T, et al. 2011. Tilførselsprogrammet 2010. Overvåking av tilførsler og miljøtilstand i Nordsjøen. NIVA rapport 6187-2011. Klima-og forurensningsdirektoratet (Klif), Rapport TA 2810/2011. ISBN 978-82-577-577-5992-3: IPCS 1992.

Heimbürger, L.-E., Sonke, J.E., Cossa, D., Point, D., Lagne, C., Laffont, L., Galfond, B.T., Nicolaus, M., Rabe, B., Rutgers van der Loeff, M.: Shallow methylmercury production in the marginal sea ice zone of the central Arctic Ocean. Scientific Rep., 5, 10318, 2015.

HELCOM. 2007. Heavy Metal Pollution to the Baltic Sea in 2004. Baltic Sea Environment Proceedings. No. 108: 33 pp.

HELCOM. 2011. Fifth Baltic Sea Pollution Load Compilation. Baltic Sea Environment Proceedings No. 128: 56 pp

Holmes, C. D., Jacob, D. J., Corbitt, E. S., Mao, J., Yang, X.,Talbot, R., and Slemr, F.: Global atmospheric model for mercury including oxidation by bromine atoms, Atmos. Chem.Phys., 10, 12037–12057, https://doi.org/10.5194/acp-10-12037-2010, 2010.

Horowitz, L. W., et al.: A global simulation of tropospheric ozone and related tracers: Description and evaluation of MOZART, version 2. J. Geophys. Res., 108, 4784-4784, 2001.

Jacovides, C.P., Tymvios, F., Papaioannou, G., Asimakopoulos, D.N., Theofilou, C.M. (2004). Ratio of PAR to broad-band solar radiation measured in Cyprus. Agricultural and Forest Meteorology 121(3):135-140

Jiskra, M., Sonke, J.E., Obrist, D., Bieser, J., Ebinghaus, R., Myhre, C.L., Pfaffhuber, K.A., Wängberg, I., Kyllönen, K., Worthy, D., Martin, L.G., Labuschagne, C., Mkololo, T., Ramonet, M., Magand, O., and Dommergue, A.: A vegetation control on seasonal variations in global atmospheric mercury concentrations. Nature Geosci., 11(4), 224-250. 2018.

Jung, G., Hedgecock, I. M., and Pirrone, N.: ECHMERITV1.0 – a new global fully coupled mercury-chemistry and transport model, Geosci. Model Dev., 2, 175–195,https://doi.org/10.5194/gmd-2-175-2009, 2009

Kuss, J.: Water–air gas exchange of elemental mercury: An experimentally determined mercury diffusion coefficient for Hg^0 water–air flux calculations, Limnol. Oceanogr., 59(5), 1461-1467, doi:10.4319/lo.2014.59.5.1461, 2014.

Kuss, J., Wasmund, N., Nausch, G., and Labrenz, M.: Mercury emission by the Baltic Sea: A consequence of cyanobacterial activity, photochemistry, and low-light mercury transformation, Environ. Sci. Technol., 49(19), 11449-11457, doi:10.1021/acs.est.5b02204, 2015.

Kuss, J., Cordes, F., Mohrholz, V., Nausch, G., Naumann, M., Krüger, S., and Schulz-Bull, D.E.: The impact of the major Baltic inflow of December 2014 on the mercury species distribution in the Baltic Sea, Environ. Sci. Technol., 51(20), 11692-11700, doi:10.1021/acs.est.7b03011, 2017.

Kuss, J., Krüger, S., Ruickoldt, J., and Wlost, K.P.: High-resolution measurements of elemental mercury in surface water for an improved quantitative understanding of the Baltic Sea as a source of atmospheric mercury, Atmos. Chem. Phys., 2018(6), 4361-4376, doi:10.5194/acp-18-4361-2018, 2018.

Kos, G., Ryzhkov, A., Dastoor, A., Narayan, J., Steffen, A., Ariya, P. A., and Zhang, L.: Evaluation of discrepancy between measured and modelled oxidized mercury species, Atmos. Chem. Phys., 13, 4839–4863, https://doi.org/10.5194/acp-13-4839-2013, 2013

Lehmann, A., and Post, P.: Variability of atmospheric circulation patterns associated with large volume changes of the Baltic Sea, Advances in Science and Research, 12, 219-225, 2015.

Mohrholz, V., Naumann, M., Nausch, G., Krüger, S., Gräwe, U., (2015) Fresh oxygen for the Baltic Sea—An exceptional saline inflow after a decade of stagnation. J. Mar. Sys. 148, pp. 152–166

Leermakers, M., Galetti, S., Galan, Da Sandra, Brion, N., Baeyens, W. (2001). Mercury in the Southern North Sea and Scheldt estuary. Marine Chemistry 75(3) 229-248.

Lehnherr, I.: Methylmercury biogeochemistry: A review with special reference to Arctic aquatic ecosystems. Environ. Rev, 22, 3, 229-243, 2014.

MARENET, https://www.bsh.de/DE/DATEN/Meeresumweltmessnetz/meeresumweltmessnetz_node.html

Mason, R.P., Reinfelder, J.R., Morel, F.M. (1996): Uptake, toxicity, and trophic transfer of mercury in a coastal diatom, Environ. Sci. Technol., 30(6), 1835–1845.

Mason, R. P., Choi, A.L., Fitzgerald, W.F., Hammerschmidt, C.R., Lamborg, C.H., Soerensen, A.L., and Sunderland, E.M.: Mercury biogeochemical cycling in the ocean and policy implications, Environ. Res., 119, 101-117, 2012.

McClelland, J.W., Holmes, R.M., Peterson, B.J., Raymond, P.A., Striegl, R., Zhulidov, A.V., Zimov, S., Zimov, N., Tank, S.E., and Spencer, R.G.: Particulate organic carbon and nitrogen export from major Arctic rivers, Global Biogeochem. Cycles, 30 (5), 629e643, 2016.

Menden-Deuer, S., and Lessard, E.J.: Carbon to volume relationships for dinoflagellates, diatoms, and other protist plankton, Limnol. Oceanography, 45(3), 569–579, 2000.

Neumann, T.: Towards a 3D-ecosystem model of the Baltic Sea. Journal of Marine Systems 25, 405-419, 2000

Niki, H., Maker, P.D., Savage, C.M., Breitenbach L.P. (1983) A long-path Fourier transform infrared study of the kinetics and mechanism for the hydroxyl radical-initiated oxidation of dimethylmercury. J. Phys. Chem. 87 (1983) 4978.

Mohrholz, V., Naumann, M., Nausch, G., Krüger, S., and Gräwe, U.: Fresh oxygen for the Baltic Sea—An exceptional saline inflow after a decade of stagnation, J. Mar. Sys., 148, 152–166, 2015.

Nfon, E., Cousins, I.T., J ̈arvinen, O., Mukherjee, A.B., Verta, M., and Broman, D.: (2009).“Trophodynamics of mercury and other trace elements in a pelagic food chain from the Baltic Sea” In:

Nightingale PD, Malin G, Law CS, Watson AJ, Liss PS, et al. 2000. In-situ evaluation of air-sea gas exchange parameterizations using novel conservative and volatile tracers. Global Biogeochem Cy14: 373–387

Obrist, D., Kirk, J.L., Zhang, L., Sunderland, E.M., Jiskra, M., and Selin, N.E.: A review of global environmental mercury processes in response to human and natural perturbations: Changes of emissions, climate, and land use, Ambio. https://doi.org/10.1007/s13280-017-1004-9, 2018.

Olenina, I., et al (2003). Biovolumes and size-classes of phytoplankton in the Baltic Sea. In: HELCOM Balt. Sea Environ. Proc., No. 106, 144 pp.607, pp. 110–114, 2003.

Pakhomova, S., Yakushev, E., Protsenko, E., Rigaud, S., Cossa, D., Knoery, J., Couture, R.l-M., Radakovitch, O., Yakubov, S., Krzeminska, D., and Newton A: Modeling the influence of eutrophication and redox conditions on mercury cycling at the sediment-water interface in the Berre Lagoon, Frontiers Marine Sci., 5, 291, doi=10.3389/fmars.2018.00291, 2018.

Parks, J.M., Johs, A., Podar, M., Bridou, R., Hurt, R.A., Smith, S.D., Tomanicek, S.J., Qian, Y., Brown, S.D., Brandt, C.C., Palumbo, A.V., Smith, J.C., Wall, J.D., Elias, D.A., and Liang, L.: Science; 339, 6125, 1332-1335, 2013.

Pickhardt, P. C., and Nicholas, S. F.; Accumulation of inorganic and methylmercury by freshwater phytoplankton in two contrasting water bodies, Environ. Sci. Technol., 41(1), 125–131, 2007.

Pirrone, N., Cinnirella, S., Feng, X., Finkelman, R.B., Friedli, H.R., Leaner, J.L., Mason, R., Munkherjee, A.B., Stracher, G.B., Streets, D.G., and Telmer, K.: Global mercury emissions to the atmosphere from anthropogenic and natural sources, Atmos. Chem. Phys., 10, 5951-5964, 2010.

Ricciardi, A., and Bourget, E.: Weight-to-weight conversion factors for marine benthic macroinvertebrates. In:Marine ecology progress series; 163, pp. 245–251, 1998.

Rosati, G. and Canu, D. and Lazzari, P. and Solidoro, C.: Assessing the spatial and temporal variability of methylmercury biogeochemistry and bioaccumulation in the Mediterranean Sea with a coupled 3D model. Biogeosciences, 19 (15) 3663 –3682.

Schartup, A.T., Qureshi, A., Dassuncao, C., Thackray, C.P., Harding, G., and Sunderland, E. M.: A model for methylmercury uptake and trophic transfer by marine plankton, Environ. Sci. Technol., 52 (2), 654–662, 2018.

Schutgens, N. A. J., Gryspeerdt, E., Weigum, N., Tsyro, S., Goto, D., Schulz, M., and Stier, P.: Will a perfect model agree with perfect observations? The impact of spatial sampling, Atmos. Chem. Phys., 16, 6335–6353, https://doi.org/10.5194/acp-16-6335-2016, 2016.

Selin, N.E., Jacob, D.J., Yantosca, R.M., Strode, S., Jaegle’, L., and Sunderland, E.M.: Global 3-D land-ocean-atmosphere model for mercury: present-day versus preindustrial cycles and anthropogenic enrichment factors for deposition, Global Biogeochem. Cycles, 22, GB2011, 2008.

Semeniuk, K., and Dastoor, A.: Development of a global ocean mercury model with a methylation cycle: outstanding issues, Global Biogeochem. Cycles, 31, 400–433, 2017.

Sicko-Goad, Linda M, Claire L Schelske, and Eugene F Stoermer (1984). “Estim.ation of intracellular carbon and silica content of diatoms from natural assemblages using morphometric techniques’”. In: Limnol. Oceanogr 29.6, pp. 1170–178.

Song, S., Selin, N. E., Soerensen, A. L., Angot, H., Artz, R.,Brooks, S., Brunke, E.-G., Conley, G., Dommergue, A., Ebing-haus, R., Holsen, T. M., Jaffe, D. A., Kang, S., Kelley, P.,Luke, W. T., Magand, O., Marumoto, K., Pfaffhuber, K. A., Ren,X., Sheu, G.-R., Slemr, F., Warneke, T., Weigelt, A., Weiss-Penzias, P., Wip, D. C., and Zhang, Q.: Top-down constraints on atmospheric mercury emissions and implications for global biogeochemical cycling, Atmos. Chem. Phys., 15, 7103–7125,https://doi.org/10.5194/acp-15-7103-2015, 2015

Soerensen A.L. and Faxneld, S. (2020) ‘The Swedish National Monitoring Programme for Contaminants in Marine Biota (until 2019 year’s data) - Temporal trends and spatial variations’, Stockholm, 2020.

Soerensen, A.L., Sunderland, E., Holmes, C.D., Jacob, D.J., Yantosca, R.M., Skov, H., Christensen, J.H., Strode, S.A., and Mason, R.P.: An improved global model for air-sea exchange of mercury: High concentrations over the North Atlantic, Environ. Sci. Technol., 44 (22), 8574-8580, 2010.

Soerensen, A.L., Schartup, A.T., Skrobonja, A., Bouchet, S., Amouroux, D., Liem- Nguyen, V., and Björn, E.: Deciphering the role of water column redoxclines on methylmercury cycling using speciation modeling and observations from the Baltic Sea, Global Biogeochem. Cycles, 32, 10, 2018.

Soerensen, A.L., Schartup, A.T., Skrobonja, A., and Björn, E.: Organic matter drives high interannual variability in methylmercury concentrations in a subarctic coastal sea, Environ. Pollut.,, 299, 531-538, 2017.

Soerensen, A.L., Jacob, D.J., Schartup, A.T., Fisher, J.A., Lehnherr, I., St. Louis, V.L., Heimbürger, L.-E., Sonke, J.E., Krabbenhoft, D.P., and Sunderland, E.M.: A mass budget for mercury and methylmercury in the Arctic Ocean, Global Biogeochem. Cycles, 30 (4), 560-575, 2016.

Soerensen, A. L., Schartup, A.T., Gustafsson, E., Gustafsson, B.G., Undeman, E., and Erik Björn, E.:Eutrophicationincreases phytoplankton methylmercury concentrations in a coastal sea—A Baltic Sea case study", Environ. Sci. Technol., 50(21), 11787–11796, 2016.

Sørland, S. L., Brogli, R., Pothapakula, P. K., Russo, E., Van de Walle, J., Ahrens, B., Anders, I., Bucchignani, E., Davin, E. L., Demory, M.-E., Dosio, A., Feldmann, H., Früh, B., Geyer, B., Keuler, K., Lee, D., Li, D., van Lipzig, N. P. M., Min, S.-K., Panitz, H.-J., Rockel, B., Schär, C., Steger, C., and Thiery, W.: COSMO-CLM regional climate simulations in the Coordinated Regional Climate Downscaling Experiment (CORDEX) framework: a review, Geosci. Model Dev., 14, 5125–5154, https://doi.org/10.5194/gmd-14-5125-2021, 2021.

Strode, S., Jaeglé, L., Selin, N.E., Jacob, D.J., Park, R.J., Yantosca, R.M., Mason, R.P., and Slemr, F.: Air-sea exchange in the global mercury cycle, Global Biogeochem. Cycles, 21, GB1017, 2007.

Streets, D.G., Horowitz, H.M., Lu, Z., Levin, L., Thackray, C.P., and Sunderland, E.M.: Five hundred years of anthropogenic mercury: spatial and temporal release profiles, Environ. Res. Lett., 14, 084004, 2019.

Sunderland, E.M., and Mason, R.P.: Human impacts on open ocean mercury concentrations, Global Biogeochem. Cycles, 21, GB4022, 2007.

Sunderland, E.M., Krabbenhoft, D.P., Moreau, J.W., Strode, S.A., and Landing, W.M.: Mercury sources, distribution, and bioavailability in the North Pacific Ocean: insights from data and models, Global Biogeochem. Cycles, 23, GB2010, 2009.

Tesán Onrubia, J. A., Petrova, M. V., Puigcorbé, V., Black, E. E., Valk, O., Dufour, A., et al. (2020). Mercury Export Flux in the Arctic Ocean Estimated from $^{234}Th/^{238}U$ Disequilibria. *ACS Earth Sp. Chem.* 4, 795–801. doi: 10.1021/acsearthspacechem.0c00055

Thunis, P., Pederzoli, A., and Pernigotti, D.: Performance criteria to evaluate air quality modeling applications, Atmos. Environ., 59, 476e482, 2012.

Thunis, P., Pernigotti, D., and Gerboles, M.: Model quality objectives based on measurement uncertainty. Part I: Ozone, Atmos. Environ., 79, 861–868. doi:10.1016/j.atmosenv.2013.05, 2013.

Travnikov, O. and Ilyin, I.: The EMEP/MSC-E Mercury ModelingSystem, in: Mercury Fate and Transport in the Global Atmo-sphere: Emissions, Measurements, and Models, edited by: Pirrone, N. and Mason, R. P., Springer, US, 571–587, 2009.

Travnikov, O., Jonson, J. E., Andersen, A. S., Gauss, M., Gusev A., Rozovskaya O., Simpson D., Sokovyh V., Valiyaveetil,S., and Wind, P.: Development of the EMEP global modellingframework, Progress report, EMEP/MSC-E Technical Report7/2009, Meteorological Synthesizing Centre – East of EMEP,Moscow, 44 pp., available at: http://www.msceast.org/index.php/publications/reports (last access: June 2017), 2009.

Tsui, M.T.K., and Wang, W.X.: Uptake and elimination routes of inorganic mercuryand methylmercury in Daphnia magna,Environ. Sci. Technol., 38(3) , 808–816, 2004.

AMAP/EMEP, 2013. Global Mercury Assessment 2013: Sources, Emissions, Releases and Environmental Transport. Geneva: UNEP Chemicals Branch.

AMAP/EMEP, 2019. Global Mercury Assessment 2018. UN Environment Programme Chemicals and Health Branch Geneva Switzerland. ISBN: 978-92-807-3744-8.

Walve, J., and Larsson, U.: (1999). "Carbon, nitrogen and phosphorus stoichiometry of crustacean zooplankton in the Baltic Sea: implications for nutrient recycling".

Wang & and Wong, 2003

Zhang, Y., Jaegle,L., and Thompson, L.: Natural biogeochemical cycle of mercury in a global three-dimensional ocean tracer model, Global Biogeochem. Cycles 28, 553–570, 2014a.

Zhang, Y., Jaegle, L., Thompson, L., and Streets, D.G.: Six centuries of changing oceanic mercury, Global. Biogeochem. Cycles, 28, 1251–1261, 2014b.

Zhang, Y., Horowitz, H., Wang, J., Xie, Z., Kuss, J., and Soerensen, A.L.: A coupled global atmosphere-ocean model for air-sea exchange of mercury: insights into wet deposition and atmospheric redox chemistry, Environ. Sci. Technol. , 53, 5052–5061, 2019.